Journal of Hydrology

Trees control hillslope subsurface flow: Insights from stemflow and throughfall experiments, geophysical surveys, and numerical modeling

--Manuscript Draft--

Manuscript Number:	HYDROL68325
Article Type:	Research paper
Section/Category:	Ecohydrology
Keywords:	Subsurface flow; Infiltration; Geophysical surveys; Stemflow; Preferential flow; Soil water repellency
Corresponding Author:	Simone Di Prima, Ph.D. University of Basilicata Potenza, ITALY
First Author:	Simone Di Prima, Ph.D.
Order of Authors:	Simone Di Prima, Ph.D.
	Gersende Fernandes
	Maria Burguet
	Maria Paz Salazar
	Elisa Marras
	Ilenia Murgia
	Konstantinos Kaffas
	Luca Peruzzo
	Ryan D. Stewart
	Majdi R. Abou Najm
	Alessandro Comegna
	Laurent Lassabatere
	Giorgio Cassiani
	Daniele Penna
	Christian Massari
	Filippo Giadrossich
Abstract:	Highlights • Subsurface flow processes were investigated at four spatial scales. • Artificial stemflow and throughfall events were conducted on a 100 m2 plot. • Numerical inverse modeling allowed soil parametrization. • A dual-permeability model accounted for preferential stemflow infiltration. • ERT and GPR imaging validated our hydrological conceptual model.

UNIVERSITÀ DEGLI STUDI DELLA BASILICATA
Dipartimento di Scienze Agrarie, Forestali, Alimentari e Ambientali

Dear Editor,

the manuscript Trees control hillslope subsurface flow: Insights from stemflow and throughfall experiments, geophysical surveys, and numerical modeling by S. Di Prima and co-authors is proposed for possible publication on Journal of Hydrology.

In this study, we investigated the effects of rainfall partitioning on subsurface water dynamics across multiple spatial scales on a 30° forested hillslope in the 'Re della Pietra' catchment, Central Italy. We considered four hierarchical spatial scales to capture subsurface water dynamics. Our findings demonstrate that the forest soil exhibits dual-domain behavior, characterized by contrasting infiltration dynamics between the matrix and fast-flow regions in response to stemflow infiltration at tree bases and throughfall infiltration between tree stems.

On the behalf of the authors

Dr Simone DI PRIMA

Highlights

- Subsurface flow processes were investigated at four spatial scales.
- Artificial stemflow and throughfall events were conducted on a 100 m^2 plot.
- Numerical inverse modeling allowed soil parametrization.
- A dual-permeability model accounted for preferential stemflow infiltration.
- ERT and GPR imaging validated our hydrological conceptual model.

Abstract

In this study, we investigated the effects of rainfall partitioning on subsurface water dynamics across multiple spatial scales on a 30° forested hillslope in the "Re della Pietra" catchment of Central Italy. Four hierarchical spatial scales were considered to capture subsurface water dynamics: the point scale (via single-ring infiltration tests at three depths), the single-tree scale (through artificial stemflow events), the plot scale (covering a 100 m² area, assessed either by an artificial throughfall event alone or in conjunction with multiple artificial stemflow events), and the hillslope scale (through piezometers data). Geophysical surveys using both Ground Penetrating Radar (GPR) and Electrical Resistivity Tomography (ERT) were also conducted at the plot and single-tree spatial scales. The infiltrometer tests were classified into concave-to-linear, concave-to-convex-to-linear, convex-to-linear, and linear shapes, which together with the use of a new analytical infiltration model for fractional wettability conditions allowed us to assess the roles of capillarity, gravity, and soil water repellency during infiltration. During the artificial throughfall event, the infiltration process was initially impeded by surface soil water repellency. Infiltration rates ultimately approached the applied rainfall intensity, with the process becoming predominantly governed by the soil matrix later on, and with limited or no influence from macropores. In contrast, artificial stemflow events revealed a rapid infiltration response around tree stems, attributable to preferential flow paths through root-induced macropores and fractures. Numerical inversions using HYDRUS-1D enabled retrieval of the soil hydraulic parameters for both the matrix and preferential flow domains. The fast-flow region beneath tree stems exhibited hydraulic conductivities up to 4.7 times higher than those of the matrix region, despite occupying only a minor fraction of the total soil porosity. Geophysical imaging corroborated these findings by revealing distinct wetting patterns from vertical infiltration beneath tree stems to lateral subsurface flow at greater depths. Integrating these diverse approaches provided a robust conceptual framework for understanding how soil water repellency and preferential flow paths interact to regulate infiltration, surface and subsurface runoff generation, and groundwater recharge on forested hillslope.

Trees control hillslope subsurface flow: Insights from stemflow and throughfall experiments, geophysical surveys, and numerical modeling

Simone Di Prima[1,*], Gersende Fernandes[2,3], Maria Burguet[4], Maria Paz Salazar[5], Elisa Marras[3], Ilenia Murgia[6], Konstantinos Kaffas[6], Luca Peruzzo[7], Ryan D. Stewart[8], Majdi R. Abou Najm[9], Alessandro Comegna[1], Laurent Lassabatere[10], Giorgio Cassiani[7], Daniele Penna[6,11], Christian Massari[12], and Filippo Giadrossich[3]

[1] Department of Agricultural, Forestry, Food and Environmental Sciences (DAFE), University of Basilicata, 85100 Potenza, Italy
[2] INRAE, UR-LEHNA, 5 Rue de La Doua, CS 20244, 69625, Villeurbanne Cedex, France
[3] Department of Agricultural Sciences, University of Sassari, Viale Italia, 39A, 07100 Sassari, Italy
[4] Institute of Agricultural Sciences, ICA-CSIC, C/ Serrrano 115b, 28006 Madrid, Spain
[5] Laboratorio de Física de Suelos (LaFiS), Facultad de Ciencias Agrarias y Forestales, UNLP, Calles 60 y 119, CC 31, 1900 La Plata, Argentina
[6] Department of Agriculture, Food, Environment and Forestry, University of Florence, Italy
[7] Department of Geosciences, University of Padua, Via G. Gradenigo, 6–35131 Padua, Italy
[8] School of Plant and Environmental Sciences, Virginia Polytechnic Institute and State University, Blacksburg, VA, United States
[9] Department of Land, Air and Water Resources, University of California, Davis, CA 95616, United States
[10] Université de Lyon; UMR5023 Ecologie des Hydrosystèmes Naturels et Anthropisés, CNRS, ENTPE, Université Lyon 1, Vaulxen-Velin, France
[11] Forest Engineering Resources and Management Department, Oregon State University, Corvallis, USA
[12] Research Institute for Geo-Hydrological Protection, National Research Council, Perugia, Italy
* Corresponding Author. E-mail: simone.diprima@unibas.it

Highlights

- Subsurface flow processes were investigated at four spatial scales.
- Artificial stemflow and throughfall events were conducted on a 100 m^2 plot.
- Numerical inverse modeling allowed soil parametrization.
- A dual-permeability model accounted for preferential stemflow infiltration.
- ERT and GPR imaging validated our hydrological conceptual model.

Abstract

In this study, we investigated the effects of rainfall partitioning on subsurface water dynamics across multiple spatial scales on a 30° forested hillslope in the “Re della Pietra” catchment of Central Italy. Four hierarchical spatial scales were considered to capture subsurface water dynamics: the point scale (via single-ring infiltration tests at three depths), the single-tree scale (through artificial stemflow events), the plot scale (covering a 100 m² area, assessed either by an artificial throughfall event alone or in conjunction with multiple artificial stemflow events), and the hillslope scale (through piezometers data). Geophysical surveys using both Ground Penetrating Radar (GPR) and Electrical Resistivity Tomography (ERT) were also conducted at the plot and single-tree spatial scales. The infiltrometer tests were classified into concave-to-linear, concave-to-convex-to-linear, convex-to-linear, and linear shapes, which together with the use of a new analytical infiltration model for fractional wettability conditions allowed us to assess the roles of capillarity, gravity, and soil water repellency during infiltration. During the artificial throughfall event, the infiltration process was initially impeded by surface soil water repellency. Infiltration rates ultimately approached the applied rainfall intensity, with the process becoming predominantly governed by the soil matrix later on, and with limited or no influence from macropores. In contrast, artificial stemflow events revealed a rapid infiltration response around tree stems, attributable to preferential flow paths through root-induced macropores and fractures. Numerical inversions using HYDRUS-1D enabled retrieval of the soil hydraulic parameters for both the matrix and preferential flow domains. The fast-flow region beneath tree stems exhibited hydraulic conductivities up to 4.7 times higher than those of the matrix region, despite occupying only a minor fraction of the total soil porosity. Geophysical imaging corroborated these findings by revealing distinct wetting patterns from vertical infiltration beneath tree stems to lateral subsurface flow at greater depths. Integrating these diverse approaches provided a robust

conceptual framework for understanding how soil water repellency and preferential flow paths interact to regulate infiltration, surface and subsurface runoff generation, and groundwater recharge on forested hillslope.

1. Introduction

Understanding the hydrological response of forested hillslopes to rainstorms is fundamental for unraveling the complex interactions between vegetation and subsurface water dynamics. Forested ecosystems play a crucial role in rainfall partitioning, as processes such as interception, throughfall, and stemflow govern the distribution of water inputs to the soil (Llorens and Domingo, 2007). Among these processes, the role of trees is particularly significant, as they influence not only the partitioning of rainfall and its movement and storage within the soil profile (Uchida et al., 2001). Trees significantly impact subsurface water dynamics, especially through the process of double-funneling. This process, characterized by the combined effect of stemflow and macropore flow pathways along root systems, facilitates concentrated water infiltration (Levia and Frost, 2003).

Recently, there has been a growing recognition of the significant role of stemflow in subsurface hydrology, with increasing attention given its capacity to influence soil water dynamics, even in species where it constitutes a relatively small proportion of total precipitation (Liang et al., 2009). Stemflow concentrates rainfall at specific infiltration points and promotes macropore flow along root systems, and may induce localized saturation (Durocher, 1990), surface and subsurface runoff generation (Neave and Abrahams, 2002), and groundwater recharge (Taniguchi et al., 1996). At sufficiently high intensities, stemflow can trigger at least one of three processes: (i) Horton overland flow, resulting from surface saturation from above; (ii) subsurface saturation above a restrictive soil layer; or (iii) rapid deep percolation along tree roots, potentially leading to the formation of a perched water table at the soil–bedrock interface (Germer, 2013).

Beech trees (*Fagus spp.*) are notable for their exceptionally high stemflow production, a characteristic associated to their smooth bark surfaces. The low surface roughness of Fagus bark minimizes water retention, thereby facilitating the efficient channeling of rainfall down the stems. This morphological characteristic enables beech trees to generate significantly higher stemflow volumes compared to rough-barked species (Levia and Frost, 2003). As a result, beech trees play a distinct role in concentrating water inputs to the soil, influencing localized infiltration and subsurface water dynamics (Hemr et al., 2023). Recently, Tischer et al. (2020) reported that stemflow infiltration at the stem base in European beech (*Fagus sylvatica* L.) was more spatially concentrated than commonly assumed, revealing a highly localized effect on water and solute dynamics in the soil profile. This concentrated water is critical in altering local soil moisture distribution and promoting macropore flow pathways (Schwärzel et al., 2012). The extensive and deep root systems of beech trees further amplify this effect by facilitating rapid water transport into deeper soil layers or even to the soil–bedrock interface. However, this stemflow also carries solute from the tree stem, which contributes to increased soil acidification near the tree base (Krueger et al., 2016) or to the shallow subsoil layers just below the main root zone, up to approximately 0.5 m in depth (Bachmann et al., 2016). This alteration in soil chemistry may further influence soil wettability, with a tendency towards greater soil water repellency as acidity increases. The appearance of soil water repellency is strongly related to SOC (Soil Organic Carbon) content and varies both temporally and spatially as other soil parameters (pH, N or texture) varies, making it a dynamic property (Dekker and Ritsema, 1994). Soil water repellency in European beech forests can significantly impact, thus, the hydrological processes within the forest ecosystem (Buczko et al., 2005; Schwen et al., 2015). Its presence can alter the way water infiltrates and moves through the soil (Doerr et al., 2000).

When studying preferential flow dynamics in soil, it is essential to clearly define the process. In this investigation, we examine different types of preferential flow, drawing on the definition provided by Gerke (2006): preferential flow describes the movement of water and solutes along specific pathways while bypassing parts of the soil matrix. Macropore flow occurs through root channels, earthworm burrows, or soil cracks, forming networks with varying geometries and dimensions, predominantly in well-structured, fine-textured soils. Unstable flow, on the other hand, is observed more common in coarse-textured soils and results from wetting front instabilities, water repellency, or air entrapment, often producing finger-like flow patterns in sandy soils. Both these processes bypass significant portions of the soil matrix, leading to complex and heterogeneous flow dynamics. Both processes bypass significant portions of the soil matrix, leading to complex and heterogeneous flow dynamics.

This renewed focus is driven by advancements in measurement techniques and geophysical tools, which now allow for more accurate and spatially resolved studies of macropore flow and stemflow-induced processes (Fan et al., 2020). Advances in geophysical techniques, such as Ground Penetrating Radar (GPR) and Electrical Resistivity Tomography (ERT), have significantly advanced our understanding of subsurface water processes. GPR provides high-resolution imaging of soil structures and root systems, while ERT offers insights into the spatial distribution of soil moisture and subsurface flow patterns. The combined application of these technologies has greatly enhanced our ability to characterize the complex processes governing subsurface water dynamics on forested hillslopes (Guo et al., 2020). Numerical modeling further complements these geophysical techniques by providing the simulation and prediction of hydrological responses under varying conditions (Liang et al., 2009). At a larger spatial scale, such as the hillslope scale, macropore flow dynamics are often identified by a relatively sudden rise in the water table, triggered by the activation of fast-flow pathways through the thickness of the vadose zone and rapidly transport rainfall to the water table (Jackisch et al., 2020). The vadose zone functions as a subsurface reservoir, modulating the temporal relationship between precipitation inputs and groundwater recharge dynamic (Vereecken et al., 2008). When matrix flow dominates in the unsaturated zone, groundwater recharge generally shows limited responsiveness to rainfall on a daily scale due to storage effects in the vadose zone that delay water movement, particularly during moderate rainfall events (Ireson and Butler, 2011). Conversely, macropore flow dynamics are associated with pronounced non-linear behavior in the timing and volume of groundwater recharge, driven by the activation of rapid flow pathways in response to effective rainfall (Lee et al., 2006).

The combination of field experiments, geophysical measurements, numerical modeling, and monitoring data offers a comprehensive approach to understanding the intricate interactions between trees and subsurface water dynamics. A key objective in studying complex phenomena like infiltration and surface and subsurface runoff generation is to understand how these hydrological processes operate across various spatial scales and to establish connections between them (Pachepsky and Hill, 2017). The primary aim of this study was to investigate the impact of rainfall partitioning on subsurface water dynamics at multiple spatial scales within a forested hillslope in central Italy. Artificial stemflow and throughfall events, combined with single-ring infiltration tests, GPR and ERT inspections, and piezometer data, were used to investigate water flow pathways across four distinct spatial scales (Figure 1): (1) the point scale, assessed through single-ring infiltration tests; (2) the single-tree scale, assessed via artificial stemflow events and ERT imaging; (3) the plot scale, assessed through artificial throughfall events alone and in combination with multiple artificial stemflow events and GPR surveys; and (4) the hillslope scale, evaluated using piezometer data. The experimental protocol was designed to provide insights into water distribution and connectivity within the

subsurface, as well as to hydraulically characterize the system using an inverse modeling approach that accounts for partitioned rainfall inputs. By integrating experimental, geophysical, and modeling approaches, this research aimed to advance our understanding of subsurface water processes, with a particular focus on the infiltration component of the water cycle.

2. Material and methods

2.1. Experimental site and plot setup

The experimental site is situated in the "Re della Pietra" experimental catchment (2 km²) in the Apennines of Tuscany, central Italy (Figure 2a). The climate in the area is characteristic of Mediterranean mountain regions, with an average annual precipitation of 1265 mm recorded over the period 2001–2021, of which 590 mm fell during the growing season (April–October). The mean air temperature is 10.5°C, with monthly variations ranging from 2°C to 20°C. The underlying lithology is composed of Macigno sandstone, a turbidite unit characterized by pelitic-dominant lithofacies and limited thickness. According to the USDA classification, the soil is Humic Dystrudepts and characterized by a high organic matter content (Fabiani et al., 2024), with a texture of sandy loam and a consistent presence of gravel. The soil depth varies from 1.5 m at the bottom of the hillslope to 0.8 m at the ridge (Verdone et al., 2025).

The studied hillslope was covered by a pure stand of beech trees. We selected a 100 m² square plot with a slope of 30°, which included eleven beech trees. We conducted the artificial stemflow events on seven of them, while the throughfall was simulated over the entire 100 m² surface (Figure 2b-c). The artificial stemflow events were conducted by applying water directly to the tree stems (see Section 2.4.2), whereas the artificial throughfall events involved supplying water beneath the canopy, directly onto the soil surface (see Section 2.4.3). For the experiments, we installed a water supply system with three PVC branches, each equipped with a ball valve to selectively control water application. The first branch supplied water to the stems of the three trees located in the upper part of the plot (Trees 1, 2, and 3), the second branch supplied water to the stems of the four trees in the lower part of the plot (Trees 4, 5, 6, and 7), and the third branch supplied water to the four sprinklers used for the artificial throughfall event across the entire plot surface. The amount of water supplied during the experiments was measured using a flow meter installed upstream of the system (Figure 2c). An electric generator and a centrifugal pump, which drew water from the Lecciona stream (Figure 2c and m), were used to supply the system. Overland flow was collected using angular aluminum profiles placed downslope of the trees and the plot (Figure 2c and k). Due to their proximity and shared root system, as they originated from the same coppice stool, downslope trees 1–2 and 6–7 were equipped with a single aluminum profile for overland flow collection (Figure 2c). The water was then channeled through flexible tubing into graduated tanks located outside the plot (Figure 2l), where the water level was recorded every 5 minutes.

A 6.5-m-long trench was also excavated, with a depth of 0.5 m at the downslope end of the plot (Figure 2c and i). Angular aluminum profiles were placed at the bottom of the trench to collect subsurface flow. During the trench excavation, a total of fifteen soil cores were collected in the trench for estimating the dry soil bulk density at depths of 0–0.1, 0.2–0.3, 0.4–0.5 m, with five cores collected for each depth. Initial water content at the time of the experiment was measured through direct measurements from soil samples collected using a hand auger at five locations across the site, two inside the plot, two along the GPR survey line, and one outside. Soil samples were taken at depths of 0–0.2, 0.2–0.4, 0.4–0.6, 0.6–0.8, 0.8–1 m, and were also analyzed to determine the particle size distribution. According to USDA standards, the soil across all five depth ranges was classified as sandy loam.

2.2. Single-ring infiltration tests and fractional wettability infiltration model

During the trench excavation, a total of fifteen single-ring infiltration tests were conducted at depths of 0, 0.2, and 0.4 m, with five tests conducted at each depth (Figure 2c and d). The tests aimed to provide point-scale estimates of saturated soil hydraulic conductivity in the soil between tree stems, specifically the area where rainfall, filtered through the canopy as throughfall, directly impacts the soil surface. Additionally, these tests aimed to identify other phenomena frequently observed in forested soils, such as soil water repellency, layering, and fractional wettability (e.g., Bachmann et al., 2016; Buczko et al., 2005; Krueger et al., 2016; Schwen et al., 2015). We used the automated infiltrometers proposed by Di Prima (2015) to infiltrate 280 mm of water, based on an infiltration surface of 1.77×10^{-2} m^2. Following the procedure prescribed by Concialdi et al. (2020), we inserted a 0.15 m inner diameter stainless steel ring a 0.01 m into the soil. The infiltrometer was then positioned inside the ring to provide water at a constant pressure head. The water height in the Mariotte reservoir was recorded using a differential transducer, which allowed the quantification of cumulative infiltration. More details about the infiltrometer can be found on the website: https://bestsoilhydro.net/infiltrometer/. Being in a beech tree forest soil, where the presence of hydrophobicity commonly occurs (both permanently and locally in space and time), small measurements following the water drop penetration time test were carried out on different locations to confirm that the process was indeed present (Wessel, 1988). At each location, we gently removed the litter and leaf residues from the soil surface and placed ten drops (0.05 mL) of distilled water onto the soil using a pipette. The drops were spaced a few centimeters apart, and the time required for each to fully infiltrate was recorded. Consequently, its presence suggests that the measured infiltration curves are likely convex or, at the very least, deviate from the typical concave-to-linear shape due to hydrophobicity.

We applied the criterion proposed by Pachepsky and Karahan (2022) to categorize cumulative infiltration curves, classifying each shape into its corresponding type. In their study, the authors identified twelve shape types, labeled from A to L, as illustrated in Figure 2 of their work. In this work, we identified the following shape types: concave-to-linear (**A** shape type), concave-to-convex-to-linear (similar to L type but with a final linear stage), convex-to-linear (**E** type), linear (**H** type), and convex-to-concave-to-linear (similar to **F** type but with a more gradual transition stage from the convex to the linear stages). Thus, the experimental curves exhibited a variety of shapes, including regular concave curves, which are indicative of fully wettable conditions, and convex curves, which suggest soil water repellency phenomena (Angulo-Jaramillo et al., 2019; Basset et al., 2025). Additionally, mixed shapes, indicative of an uneven distribution of hydrophobic material on the soil infiltration surface (Di Prima et al., 2025), were also observed. The variability in the shapes of the collected infiltration dataset posed challenges for conventional models, which only account for regular concave shapes (Abou Najm et al., 2021). To address this diversity, we selected an infiltration model recently proposed by Di Prima et al. (2025). In line with these authors, we conceptualized the soil as exhibiting a fractional wettability (FW) configuration, characterized by two distinct fractions: (1) a soil water-repellent (WR) fraction, in which hydrophobic effects initially hinder water infiltration and then diminish through time, resulting in convex-shaped cumulative infiltration curves; and (2) a wettable (W) fraction, where capillary and gravitational forces dominate, leading to a decreasing infiltration rate until a steady-state is achieved, which is characterized by concave-shaped cumulative infiltration curves. Using this model, we could estimate hydraulic parameters from curves exhibiting all observed shapes, including both concave and convex shapes, as well as mixed forms such as concave-to-convex and convex-to-concave.

Assuming the presence of a discrete repellent layer at or just below the soil surface that covers some portion of the infiltration area, water infiltration into the fractional wettable soil, $I_{\mathrm{FW}}(t)$, was modeled by the following equation (Di Prima et al., 2025):

$$I_{\mathrm{FW}}(t) = I_{\mathrm{W}}(t) \times w_{\mathrm{FW}} + I_{\mathrm{WR}}(t) \times (1 - w_{\mathrm{FW}}) \qquad 0 \le w_{\mathrm{FW}} \le 1 \qquad (1)$$

where $I_{\mathrm{W}}(t)$ is the three dimensional (3D) cumulative infiltration into the wettable fraction, $I_{\mathrm{WR}}(t)$ is the 3D cumulative infiltration into the water-repellent fraction, and the subscripts W and WR respectively refer to wettable and soil water-repellent. The parameter w_{FW} represents the fraction of the total water volume infiltrating into the wettable soil. Consequently, $(1 - w_{\mathrm{FW}})$ represents the remaining volume fraction of water infiltrating through the soil water-repellent surface. The parameter w_{FW} expresses the relative importance of the forces interacting in the fractional wettability soil (Di Prima et al., 2025).

Using the transient infiltration equation proposed by Lassabatere et al. (2006) for concave-shaped curves to model $I_{\mathrm{W}}(t)$, and the equation proposed by Di Prima et al. (2021) for convex-shaped curves to model $I_{\mathrm{WR}}(t)$, Eq. (1) becomes:

$$I_{\mathrm{FW}}(t) = \left\{S\sqrt{t} + [A(1-B)S^2 + Bi_{\mathrm{s}}]\, t\right\} \times w_{\mathrm{FW}} + \left\{S\sqrt{t} - \frac{S\sqrt{\pi}}{2\sqrt{\alpha_{\mathrm{WR}}}} erf\left(\sqrt{\alpha_{\mathrm{WR}} t}\right) + [A(1-B)S^2 + Bi_{\mathrm{s}}]t - \frac{[A(1-B)S^2 + Bi_{\mathrm{s}}](1 - e^{-\alpha_{\mathrm{WR}} t})}{\alpha_{\mathrm{WR}}}\right\} \times (1 - w_{\mathrm{FW}}) \qquad (2)$$

where $(1 - e^{-\alpha_{\mathrm{WR}} t})$ is an exponential scaling factor proposed by Abou Najm et al. (2021) to modify the infiltration rate for better simulations of water-repellent conditions, α_{WR} (T^{-1}) is an empirical parameter that reflects the rate of soil water repellency attenuation during infiltration, t(T) is the time elapsed since the start of the infiltration test, S ($\mathrm{LT}^{-0.5}$) is the soil sorptivity, i_{s}(LT^{-1}) is the steady-state infiltration rate, B is a coefficient that can be set equal to 0.467 for most soils with dry initial conditions (Di Prima et al., 2016), and A (L^{-1}) $= \gamma / r(\theta_s - \theta_i)$, where r(L) is the radius of the infiltration source, θ_{s}($\mathrm{L^3L^{-3}}$) and θ_{i}($\mathrm{L^3L^{-3}}$) are the saturated and initial volumetric soil water contents, and γ is a shape parameter for geometrical correction of the infiltration front shape, which is commonly set to 0.75 (Haverkamp et al., 1994).

2.3. Artificial throughfall and stemflow events

2.3.1. Timeline of the artificial events

The artificial throughfall and stemflow events aimed to assess the contribution of beech trees to subsurface flow generation and dynamics. Figure 3 illustrates the timeline of artificial stemflow and throughfall events. The adopted strategy aimed to measure infiltration and runoff rates induced by each simulated process: stemflow alone (depicted in blue), throughfall alone (depicted in brown), or the combined effect of both stemflow and throughfall (depicted in blue with brown stripes). The artificial events were conducted on the 26$^{\mathrm{th}}$ and 27$^{\mathrm{th}}$ of July 2023. On both days, we first conducted artificial stemflow events on the seven selected beech trees. For these experiments, the water application consisted of two stages. In the first stage, we applied water to the trees located in the upper part of the plot (Trees 1, 2, and 3). In the second stage, water was applied to the trees located in the lower part of the plot (Trees 4, 5, 6, and 7). On the first day, after the artificial stemflow events, we conducted the artificial throughfall event on the 100 m² plot. On the second day, the stemflow experiments were followed by simultaneous throughfall and stemflow events, carried out on the seven trees at the same time.

2.3.2. Characteristics of the artificial stemflow events

To setup the artificial stemflow experiment on each tree, we followed the procedure described in Di Prima et al. (2023, 2022). Water was applied using a PVC pipe with 1-mm-diameter holes spaced every 50 mm along the side facing the stem. The pipe was connected to a plastic funnel and positioned around the tree stem at 0.2 m from the soil surface. During the experiment, water was applied to each tree stem using pressure-compensated sprinklers (SuperNet UDK manufactured by Netafim^{TM}), with a declared flow rate of 58 L h^{-1} for a pressure range between 1.5 and 4 bar, placed inside the funnels (Figure 2c and f-h). The effective amount of water applied to the tree stems over 1.75 hours varied between 116.3 and 126.3 L. This amount of water corresponded to the expected volume collected by the tree crowns for a rainfall intensity between 106.9 and 132.5 mm h^{-1} and represented a stemflow rate of 7.0% (Table 1), as reported for a similar beech stand (Staelens et al., 2008). With these experiments, our aim was to reach the critical capacity of the tree-soil system to induce overland flow and measure stemflow infiltration at its maximum rate.

2.3.3. Characteristics of the artificial throughfall events

The artificial throughfall events were conducted using four rotary sprinklers (MegaNet^{TM} 24D manufactured by Netafim^{TM}) positioned at each side border of the 100 m^2 square plot. The sprinklers had a nominal flow rate of 230 L h^{-1} at an imposed pressure of 3 bar and were mounted on road guards to achieve 180° wetted areas. The actual throughfall intensity, I_T (mm h^{-1}), was 8.04 mm h^{-1}, estimated using ten rain gauges placed within the plot on the second day during the final hour of the throughfall simulation event. The total simulated throughfall heights were 41.6 mm over 5 hours and 10 minutes on the first day, and 45.6 mm over 5 hours and 40 minutes on the second day. These amounts of water corresponded to incident rainfall heights of 58.5 mm and 64.2 mm, respectively, considering a throughfall-precipitation ratio of 71%, as reported at the Lecciona experimental site for the growing season (Verdone et al., 2025), with an intensity for both the gross events of 11.3 mm h^{-1} (Table 1). The artificial events had return periods approximately between 10 and 20 years (Appendix A) (sir.toscana.it).

2.3.4. Estimation of stemflow infiltration rates

The stemflow infiltration rates, *SIR* (mm h^{-1}), were estimated using two different procedures, depending on the spatial scale considered: on the one hand the tree spatial scale , and the 100 m² plot spatial scale on the other hand (Table 2, Procedures 1 and 2). For both spatial scales, the acquisition time interval, Δt, was set to 5 minutes, based on the frequency of water level measurements in the graduated tanks used to collect and store overland flow (Figure 2l). Steady-state conditions during the infiltration processes were evaluated by identifying the final linear portion of the cumulative volume versus time plots, which corresponded to the stabilization of the infiltration rates.

2.3.4.1. Procedure 1: *SIR* estimation at the tree spatial scale

For each tree, the stemflow infiltration volume, *SIV* (L) (Table 2, Procedure 1, Step 3), was calculated by subtracting the overland flow volume, OV_{TREE} (L) (Step 1.2), collected using the angular aluminum profiles placed downslope of the tree, from the stemflow volume, SV_{TREE} (L) (Step 1.1), which was applied to the tree stem using the sprinkler. The infiltrated volume was then converted into stemflow infiltration height, SIH_{TREE} (mm) (Step 1.6), by considering an infiltration area at the soil surface equal to the tree's basal area, *ABT* (m^2) (Step 1.5). This corresponds to an infiltration buffer area around the tree with a length, L_{BUFFER} (m), calculated as $r_B \times (\sqrt{2}-1)$, where r_B (m) is the radius at the base of the tree. This assumption is consistent with the cross-section area of the wetting zone observed below Tree 5 during ERT monitoring (see Section 3.4). The mean L_{BUFFER} value for the seven trees was 0.05 m, aligning with the wet patterns observed around the stems where runoff was

absent. The plot of SIH_{TREE} as a function of time showed that a steady state was reached after 0.5 hours for most trees. Then, the steady-state stemflow infiltration rates ($SIR_{ST\text{-}TREE}$, mm h^{-1}) (Step 1.7), were determined by considering a final steady stage of 0.5 hours (Step 1.4).

2.3.4.2. Procedure 2: *SIR* estimation at the 100 m^2 plot spatial scale

At the plot scale, the steady-state stemflow infiltration rate, $SIR_{ST\text{-}PLOT}$ (mm h^{-1}) (Table 2, Procedure 2, Step 10) was calculated from the artificial event conducted on the second day (7/27/2023, 12:25–18:05), when both throughfall and stemflow processes were active. The infiltration volume, IV_{PLOT} (L) (Step 2.5), which included both throughfall and stemflow components, was calculated subtracting the overland flow volume, OV_{PLOT} (L) (Step 2.4), collected using angular aluminum profiles placed downslope of the plot, from the applied volume, V_{PLOT} (L) (Step 2.1), measured by means of a flowmeter (Figure 2c). We then calculated the stemflow infiltration volume, SIV_{PLOT} (L) (Step 2.6), by subtracting the throughfall volume, TV_{PLOT} (L) (Step 2.3), which was estimated based on the intensity of the throughfall component (step 2.2, see Section 2.4.3), from IV_{PLOT}. This procedure assumed that, as observed on the first day, all the throughfall also infiltrated during the second day, and the throughfall overland flow volume was negligible (see Section 3.5). The stemflow infiltration height, SIH_{PLOT} (mm) (Step 2.9), was then calculated by considering an infiltration surface, *ABTs* (m^2) (Step 2.8), equal to the sum of the trees' basal areas. Finally, the value of $SIR_{ST\text{-}PLOT}$ (Step 2.10) was determined by considering a steady stage of 2 hours (Step 2.7).

2.4. ERT surveys and data processing

Time-lapse ERT measurements were conducted using a high-resolution 3D setup (Binley et al., 2015; Cassiani et al., 2016, 2015). The setup was designed to maximize the ERT resolution within a cuboid of 1.2 × 1.2 × 1.2 m (Appendix B). A total of 72 electrodes were used: 24 on the surface and 48 equally distributed across four boreholes. The boreholes were installed at the edges of the cuboid, and the 12 electrodes were spaced 10 cm. The 24 surface electrodes were deployed on a regular 5 × 5 grid, skipping one electrode in the center of the grid (Mary et al., 2020, 2018; Peruzzo et al., 2024, 2020). The ERT setup was centered on Tree 5. The position of the tree stem corresponded to the missing electrode. The subpanel a in Appendix B shows the 3D setup and the position of the 72 electrodes, highlighted by the black spheres and maxima of sensitivity (red colors). The figure also highlights the irregular surface slope within the ERT setup. This irregular morphology was mapped by measuring the relative heights of the surface electrodes and heads of the boreholes. The heights were then triangulated to generate the 3D mesh used in the ERT inversion. The mesh was refined to a minimum size of 3 cm around the electrodes using a three-dimensional finite element mesh generator, Gmsh (Geuzaine and Remacle, 2009). The ERT data were processed based on the reciprocal error, removing all measurements with reciprocal error larger than 10 %. The data were then inverted with PyGIMLi Python library (Rücker et al., 2017). The time-lapse inversion used a full coupled 4D scheme, whence all the datasets were inverted at once to minimize the model variability both in time and 3D space (Wilkinson et al., 2022). The inverted models were then visualized as resistivity (Figure in Appendix B, subpanel b) and percentage change between consecutive time steps. A total of 22 datasets were collected, 19 during the two days of field experiments to evenly cover the resistivity changes induced by the water inputs, and 3 additional datasets the day before to verify the correct functioning of the setup.

2.5. Time-lapse GPR surveys and data processing

In this study, the GPR survey line was surveyed twice: once before and once after stemflow and throughfall experiments, to identify flow pathways and their respective depths. The experiments were

conducted at the plot scale, with the GPR survey line strategically positioned beneath the experimental area. Prior to the infiltration experiments, when the soil was dry, a GPR survey was conducted along a designated line using a GSSI (Geophysical Survey System Inc., Salem, NH) SIR 3000 system with a 900-MHz antenna. A time window of 50 ns was chosen to target the top 4 m of the soil, as lateral flow was anticipated to occur at depth (Fabiani et al., 2024). On the morning of July 28th, the day after the final water supply, the GPR survey line was resurveyed to assess changes induced by lateral flow. During these experiments, minimal surface overland flow was observed, suggesting the predominance of subsurface/more-in-depth flow processes. The two GPR radargrams were then processed using Reflexw software (version 9.5, Sandmeier Scientific Software, Karlsruhe, Germany). The data processing workflow included the following steps: (i) gain correction in the field setup to compensate for signal attenuation with increasing depth, (ii) application of a static time shift to align the direct ground wave arrivals to 0 ns based on identified peaks, (iii) background removal to enhance data clarity by reducing unwanted noise, and iv) running average and horizontal smoothing to suppress trace-dependent noise. The depth, D (L), was determined from the wave travel time obtained through GPR acquisition, considering the wave velocity estimated from the detection of a buried object at a known depth. A metal piece was buried at a known depth, and the two-way travel time, T (T) at the hyperbola vertex was measured. The wave velocity was then calculated as $V = 2D / T$, yielding a value of 0.183 m/ns, which corresponds to a dielectric constant of 2.7.

2.6. Numerical inversions

Water flow within the one-dimensional (1D) soil profile was simulated using HYDRUS-1D (Šimůnek et al., 2024). The absence of subsurface flow at the excavated trench on the downslope side of the plot provided evidence of the lack of significant lateral movement within the upper 0.5 m of soil. Similarly, other authors have reported predominant vertical movement of stemflow, leading to the formation of saturated zones extending to the water table (Durocher, 1990). These observations justify the use of a 1D modeling approach to capture the dominant vertical flow processes in the study area. According to Sansoulet et al. (2008), stemflow and throughfall were used as atmospheric boundary conditions at the soil surface of the domain. Since both the ERT and GPR surveys indicated predominant vertical water movement within the first 1 m of soil during the stemflow artificial experiments (see Sections 3.1 and 3.2), the depth of the soil profile was set accordingly, with free drainage as the lower boundary condition. The initial, final and saturated water contents, measured in the field, were used in the simulations. We used the inverse option in HYDRUS-1D to retrieve the soil hydraulic parameters from artificial throughfall and stemflow events, as illustrated in Appendix C. According to Crabtree and Trudgill (1985), the main hypothesis underlying the numerical simulations was that stemflow infiltrated through macropores, bypassing the matrix, while the infiltrated throughfall primarily moved into the soil matrix. This strategy allowed us decouple macropore and matrix flows and to adopt the appropriate hydraulic model depending on the modeled process. Specifically, for modeling the throughfall artificial experiment on the first day, we used the single porosity model by van Genuchten-Mualem (1980), while for modeling stemflow infiltration, we applied the dual-permeability model by Gerke and van Genuchten (1993). For the latter, the values of α and n were chosen arbitrarily to represent fast-flow regions characterized by low capillarity and predominantly gravity-driven flow. In addition, we assumed a low effective hydraulic conductivity of 0.1 mm h^{-1} at the macropore-matrix interface, meaning that water exchange between macropores and the surrounding soil matrix was assumed to be highly restricted. Consequently, infiltration into the matrix remained minimal, causing water to bypass the soil structure through macropores, where macropore flow dominated and accelerated deep percolation. The hydraulic parameters retrieved from these experiments were then used as inputs for the dual-permeability model to invert the

experimental infiltration data from the second day, when both throughfall and stemflow infiltrations were active.

The adequacy of model fits was evaluated based on the consistency of the model shape and the fit relative error, Er_{FIT}, which was estimated as follows:

$$Er_{\mathrm{FIT}} = 100 \times \sqrt{\frac{\sum_{i=1}^{n}\left(x_i^{exp} - x_i\right)^2}{\sum_{i=1}^{n}\left(x_i^{exp}\right)^2}} \quad (3)$$

where n is the total number of data pairs, x_i^{exp} are the experimental data and x_i are the values predicted by the models. Values of $Er_{\mathrm{FIT}} < 5\%$ were assumed to indicate a satisfactory inversion procedure (Angulo-Jaramillo et al., 2016; Lassabatere et al., 2006).

2.7. 2D numerical simulation

The transect dimensions were set to study the spatially redistributed stemflow under Tree 5, which had been monitored with ERT. Water flow within the two-dimensional (2D) soil profile was simulated using HYDRUS-2D/3D (Šimůnek et al., 2024). For this simulation, we used the dual-permeability model by Gerke and van Genuchten (1993). The transect slope was set to 30°, and the transect length along the slope was 3 m. An impermeable barrier, schematically representing the tree stem, was placed in the middle of the transect, with a stem diameter of 0.293 m (Nikodem et al., 2010). The soil properties obtained from the numerical inversion were applied to the 2D simulation, with the same material distribution applied. The stemflow infiltration flux was applied around the stem, with a buffer of 0.06 m. The soil profile depth was set to 1 m, with free drainage as the lower boundary condition. Similar initial conditions were applied as for the simulation in 1D.

2.8. Groundwater-level dynamics

Piezometer data were used to identify fast-flow pathways at the hillslope spatial scale by detecting sudden rises in the water table (Jackisch et al., 2020). We referred to the piezometer data published by Macchioli Grande et al. (2024), which spanned period from 19 January 2021 to 20 January 2022. We used the data recorded from the wells labeled GW1, GW2 and GW3 in their study. Groundwater levels were measured using pressure transducers with a recording interval of 15 minutes. Wells GW1 and GW3 were installed 1 and 3 m from the Lecciona stream, in a relatively flat area of the riparian zone (14°). GW2 had the deepest water table, located 1–2 m deeper than the other two wells. It was installed at the footslope, slightly elevated in altitude, 12 m from the stream, with a local slope of 26°.

3. Results

3.1. Soil infiltration capacity and surface soil water repellency

The 15 infiltrometer tests at three depths provided point-scale estimates of saturated soil hydraulic conductivity (K_s) throughout the soil profile. In addition, these tests enabled the quantification of phenomena such as water repellency and fractional wettability (Table 3). According to the criterion proposed by Pachepsky and Karahan (2022), we classified the cumulative infiltration curves into five shape types. Types A (concave-to-linear, i.e., regular shape) and L (concave-to-convex-to-linear) were the most common, each represented by six curves. The former represents the typical shape occurring when capillarity and gravity are the dominant forces controlling the process (Angulo-Jaramillo et al., 2019), while the latter is indicative of fractional wettability phenomena, reflecting the uneven distribution of hydrophobic material on the soil surface (Di Prima et al., 2025).

Fractional wettability conditions predominated at the soil surface, with four curves showing mixed shapes: three of the L type and one of the F type (convex-to-linear shape with non-monotonous infiltration rate). For these tests, the influence of water-repellent fractions was more pronounced than in the underlying layers, with higher impedance phenomena. This was reflected in a mean α_{WR} value of 16.7 h^{-1}, with greater water-repellent fractions ($1 - w_{FW}$) in the surface layer than in the subsurface, ranging from 0.6 to 0.7.The remaining curve exhibited a convex-to-linear shape (E type), typically associated with severe soil water repellency conditions (Angulo-Jaramillo et al., 2019). For this curve, Eq. (2) produced the lowest α_{WR} (2.2 h^{-1}) and highest ($1 - w_{FW}$) (0.8) values in the dataset. We obtained a mean K_s value of 177.8 mm h^{-1} at the soil surface.

Four out of five curves measured at a depth of 0.2 m displayed the A shape type, while the remaining curve exhibited a linear shape (E type), indicative of a primarily gravity-driven process. Overall, at this depth, the soil exhibited predominantly wettable conditions, associated with higher values of the w_{FW} parameter compared to the soil surface, ranging between 0.4 and 0.7, and a mean K_s value of 237.4 mm h^{-1}.

Predominantly wettable conditions were also detected at a depth of 0.4 m, where two curves exhibited the A-type shape, while the other three fell within the L-type, showing gentler convex shapes compared to the L-type curves at the soil surface. This result is likely due to the moderate influence of water-repellent fractions, as indicated by higher w_{FW} and α_{WR} values for these three curves. At this depth, we obtained a mean K_s value of 224.6 mm h^{-1}, very close to those of the layers above. In conclusion, as anticipated, soil water repellence was strongest at the soil surface and diminished with increasing depth.

3.2. Artificial throughfall event on Day 1

As measured during the artificial event on Day 1, the actual intensity of the throughfall component, I_T, was 8.04 mm h^{-1}. This value was much lower than the infiltration capacity of the studied soil, which was quantified using infiltrometers and measured at the soil surface as 117.8 mm h^{-1}. During the last 2 hours of the artificial throughfall event on the first day, we observed the stabilization of the infiltration rate at 7.98 mm h^{-1} (Figure 4b), a value very close to I_T, with a corresponding overland flow rate of only 0.06 mm h^{-1}. Overall, only the 1.3% of the sprinkled water volume generated overland flow (Figure 4c).

From an accurate inspection of the infiltration rates (Figure 4b), we also observed a slight increasing trend from 45 minutes to the third hour, before the final stabilization. This trend, associated with the maximum overland flow rate measured during the experiment, was attributed to soil water repellency at the soil surface, as suggested by the analysis of the infiltrometer data. Soil water repellency impeded infiltration during this stage and diminished gradually as the soil became wetter (DeBano, 2000), leading to the final stabilization of the process occurring three hours after the beginning of the experiment. During the first three hours, we collected 75% of the total overland flow, suggesting that soil water repellency and, consequently, the actual soil water content play a significant role in the generation of overland flow.

3.3. Artificial stemflow events on Days 1 and 2

The figure in Appendix D illustrates the cumulative volumes and rates versus time plots of the applied stemflow, as well as the collected overland flow and calculated infiltration. With the sole exception of the artificial stemflow event on the second day for Trees 1-2, we consistently applied water at rates higher than the soil infiltration capacity around the stems, ensuring that stemflow

infiltration was measured close to its maximum rate. For Trees 1 to 4, we observed a slight increase in infiltration rates from the first to the second day, while the opposite trend was noted for Trees 5 to 7. Overall, for each tree, the repeated experiments over the two days yielded similar amounts of infiltration, ranging from 37.2% (Tree 5, Day 2) to 100% (Trees 1-2, Day 2) of the total applied stemflow volume, suggesting good replicability of the experiments and a degree of independence from initial conditions for a given tree. It should be noted that Tree 5 produced the highest overland flow rates, with only 40.6% and 37.2% of the applied water infiltrating at the stem base on the first and second days, respectively. This result is not surprising, given that the installation of the electrodes likely caused a disturbance in the soil volume, particularly leading to compaction at the soil surface. Nonetheless, the percentage of infiltrated water remained high for all the other trees, highlighting that only exceptionally high stemflow inputs are capable of inducing overland flow at the soil surface.

The steady-state condition of the infiltration process was evaluated by identifying the final linear portion of the cumulative volume versus time plots, where the infiltration rates stabilized. Specifically, we considered the final steady stages of 0.5 hours. At steady state, infiltration rates ranged from 0.42 to 2.39 L min^{-1}, depending on the tree, while the steady-state stemflow infiltration rates, $SIR_{ST\text{-}TREE}$, ranged from 372.7 to 1663.1 mm h^{-1}, with a mean value of 1031.9 mm h^{-1} (Figure 5a).

3.4. Insights from ERT monitoring at the tree spatial scale

The 22 time-lapse ERT datasets were acquired and processed as described. The initial tests confirmed the correct functioning of the setup, including the order of the electrodes and good electrical contact of the electrodes. The highest contact resistances were measured on 4 borehole electrodes and were around 30 kΩ. The data quality remained good over the entire monitoring period. Based on the reciprocity check, an average of 10 % of the data were removed from the initial sequence of 9936 measurements. Considering the numerousness of the sequence, the remaining measurements ensured the stability and resolution of the ERT inversion. Subpanel b of the figure in Appendix B shows the background resistivity model from the morning of the first day of field experiments, before the beginning of the stemflow simulation. The figure captures a shallow and more conductive region (500 Ω m) that corresponds to the proximal part of the root system. The resistivity increases downwards and reaches values of 4000 Ω m. This resistivity increase is particularly evident in the downhill portion of the 3D volume, which highlights a lateral variability induced by the interplay between plant roots and subsurface hydro-mechanical properties. The relative high resistivities and their vertical profile agree with a variably fractured-altered sandstone and a more conductive coverage with sandy sediments and organic matter (Amendola et al., 2016; Fabiani et al., 2024).

Figure 6 shows the percentage differences between the beginning and end of the four water inputs. The 3D models are clipped with a plane passing at x = 0.6 m, exposing the central part of the volume and half of its downhill face. Figure 6a shows the resistivity changes associated with the first stemflow experiment. The resistivity changes were concentrated in the central downhill portion, i.e., just downhill of the plant stem. Vertically, the changes were more significant in the shallow part and decrease with depth, around 50 % in the top 20 cm and 20 % in the deep part. The verticality of the infiltration is highlighted by the limited changes in the uphill portion of the 3D volume. Figure 6b illustrates the changes induced by the afternoon artificial throughfall event on the first day, following the stemflow experiment. The changes were significantly different with respect to the stemflow ones. In particular, the changes concentrated in the downhill lateral regions, which had not been affected by the stemflow infiltration. The infiltration is also shallower, limited to the top 60 cm. In addition, some changes were also visible in correspondence of the tree stem, which was also not affected by

the stem flow. It is possible that water input from the uphill areas infiltrated when reaching the plant. The second stemflow simulation (morning of Day 2) led to resistivity changes that were similar to the stemflow experiment of the previous day, i.e., concentrated in the central and downhill region (Figure 6c). This result highlights how similar infiltration paths were activated by the two stemflow events, despite the different moisture contents. Figure 6d shows the changes induced by the last experiment, which combined both stemflow and rain simulation. The induced changes affected the entire investigated region, indicating the both flow paths were activated. The fact that additional changes were visible also indicates that more water accumulated during this last experiment. In this sense, the proximal part of the root system represents the only exception, as the ERT monitoring captured no changes. The maximum water holding capacity likely had already been reached in that region, possibly in line with the lower resistivities captured by the background measurements (Figure in Appendix B, subpanel b). On the contrary, significant changes were visible in the deep part, with large portions exceeding 50%, indicating that the substantial water input was only partially retained by the shallow part.

3.5. Insights from the joint throughfall and stemflow simulations events on Day 2

On the second day, the combined throughfall and stemflow simulations were designed to mimic a more realistic infiltration process occurring during natural storms, where incident rainfall reaches the soil surface partitioned as throughfall and stemflow. A comparison between this experiment and the simulation on Day 1, which included only the throughfall component, led to the following considerations:

- Almost all the throughfall component applied during the second-day simulation infiltrated into the soil. The intensity of the throughfall component was much lower than K_s measured throughout the soil profile (Table 3). On the first day, this feature resulted in steady infiltration rates closely matching the applied rainfall intensity (Figure 4b). Thus, we can reasonably hypothesize that a similar dynamic occurred on Day 2. Additionally, wetter initial conditions on Day 2 likely reduced infiltration impediments caused by surface soil water repellency.
- Almost all the overland flow collected during the second-day simulation was generated at the trees base from the stemflow component. Although we observed a high infiltration capacity around the stems, the stemflow simulation events were designed to exceed this capacity to induce overland flow, thereby measuring stemflow infiltration at its maximum rate, while still reflecting realistic and plausible rainfall events.

From these considerations, we can reasonably assume that the fraction of surface flow infiltrating at the tree bases can be estimated by subtracting the total applied throughfall from the measured total infiltration (see Section 2.3.4.2), yielding a value of 35.2 %, which was subsequently implemented in the double-permeability model in HYDRUS-1D (see Section 4.4 and the flowchart in Appendix C). This assumption also allowed for the estimation of the steady-state stemflow infiltration rate at the plot scale (Table 2, Procedure 2, Step 6), yielding a $SIR_{ST\text{-}PLOT}$ value of 1065.1 mm h^{-1} (Figure 5b).

3.6. Soil parameterization through numerical inversion

The first objective of the numerical inversions was to separately estimate the soil hydraulic properties of these two soil regions using infiltration data from the artificial throughfall and stemflow events conducted on the first day. To characterize the matrix region between the tree stems, we inverted the artificial throughfall event and used the single-porosity model by van Genuchten-Mualem (1980). Figure 7a illustrates the HYDRUS-1D model adapted to the experimental cumulative

infiltration curve (Day 1, 12:35 AM–5:45 PM); the fitted parameters are reported in Table 4. The resulting K_s value was 217.5 mm h^{-1}.

To characterize the fast-flow region beneath the tree stems, we inverted the artificial stemflow events and used the dual-permeability model by Gerke and van Genuchten (1993). The parameters retrieved from the inversion of the throughfall infiltration data were used to characterize the matrix region and were kept constant during the fittings (flowchart in Appendix C). The figure reported in Appendix E illustrates the HYDRUS-1D model adapted to the experimental cumulative infiltration curves (Day 1, 08:30 AM–12:05 AM). The inversion procedure resulted in accurate fits of the model to the experimental data, with Er_{FIT} values ranging from 0.64% to 1.86%. The obtained K_s values ranged from 404.2 to 1,636.5 mm h^{-1}, with a mean value of 1,032.9 mm h^{-1}.

4. Discussion

4.1. Effects of soil water repellency and fractional wettability on infiltration

During the artificial throughfall event on Day 1, the initial stage of the infiltration process was characterized by a decline in infiltration rates over time, due to the gradual attenuation of capillary forces as the wetting front advanced deeper into the soil. According to the fractional wettability concept proposed by Di Prima et al. (2025), the three detected stages differed by the relative importance of the factors—capillarity, gravity and water impedance—interacting during the process. Specifically, during the first stage, the decrease in infiltration rates was attributed to the rapid attenuation of capillarity in the wettable fraction. In the second stage, infiltration rates gradually increased as water impedance diminished in the water-repellent fraction. Then, the cumulative infiltration curves approached linearity, with gravity becoming the dominant force driving downward flow through both soil fractions. Macroscopically, the evolution during the infiltration process of these reciprocal interactions shaped the thoughtful cumulative infiltration curve as concave-to-convex-to-linear.

A similar dynamic was also observed at the soil surface during the infiltration tests. Although we did not detect significant differences in K_s values across the three depths, suggesting a consistently high infiltration capacity throughout the soil profile, differences emerged in terms of soil wettability under dry conditions. The hydraulic response in the surface layer reflected the uneven distribution of water-repellent materials, as typically expected in forested soils, including those beneath beech stands (e.g., Buczko et al., 2005). This similarity between the two spatial scales—the infiltrometers at the point scale and the artificial throughfall event at the 100 m^2 scale—reinforce the validity of our interpretation and the robustness of the adopted fractional wettability infiltration model. Both experiments yielded similar K_s values, which can be considered representative of the soil between tree stems—specifically, the area where rainfall, filtered through the canopy as throughfall, directly interacts with the soil surface.

During the artificial stemflow events, a slight increase in infiltration rates was observed only in some experiments (Day 1: Trees 1-2, 3, 4, 5; Day 2: Tree 5). We attribute this to soil surface repellency, which impeded infiltration during the initial stages of water supply, as also observed in the infiltrometer data and the throughfall simulation on the first day. For these same trees, the absence of an increasing trend during the simulations on the second day corroborates this hypothesis, as higher water content typically reduces the effect of soil water repellency (Doerr and Thomas, 2000). However, given that similar amounts of stemflow infiltrated over the two days, this process does not appear to be particularly significant. This likely occurs because stemflow infiltrated preferentially

around the stems (Levia and Frost, 2003), bypassing the matrix and thereby minimizing the impact of soil water repellency-related impediments (Di Prima et al., 2021).

Overall, these results suggest that soil water repellency can promote fingered flow and hinder water infiltration during the early stages of wetting, especially under initially dry conditions. This effect was evident during the infiltrometer tests and the artificial throughfall and stemflow events on the first day, when the actual volumetric soil water content was 0.17 m^3 m^{-3}. Under the specific circumstance of fractional wettability, the accurate interpretation of the infiltration processes required a careful examination of the curve shape, while modeling water infiltration at the point scale also demanded the determination of the extent of the fractional phenomena and knowledge of both the α_{WR} and w_{FW} parameters.

4.2. Rapid flow pathways beneath tree stems

Overall, the results from the artificial stemflow and throughfall events, along with the infiltrometer tests and geophysical findings, facilitated the development of a conceptual model for the studied forest soil. Specifically, we conceptualized the hillslope as consisting of two regions: a fast-flow region beneath the tree stems, dominated by fast vertical fluxes, characterized by macropores or fractures connected to the soil surface that facilitate the rapid infiltration of stemflow; and a region dominated by matrix flow between the tree stems, where rainfall arriving at the soil surface as throughfall infiltrates at slower infiltration rates. In accordance with several other studies, this conceptualization views trees as hydrologically active agents, with their stems acting as initiation points from which water inputs from stemflow can rapidly infiltrate and, in the absence of a restrictive layer, deeply percolate via preferential flow paths bypassing the soil matrix (e.g., Durocher, 1990; Guo et al., 2020; Johnson and Lehmann, 2006; Liang, 2020; Schwärzel et al., 2012; Spencer and van Meerveld, 2016; Uchida et al., 2001). This conceptual model is supported by the high steady-state stemflow infiltration rates ($SIR_{ST\text{-}TREE}$) observed during the artificial stemflow events, underscoring the soil's remarkable capacity to infiltrate water around the stems through rapid macropore flow, which bypasses the soil matrix (Crabtree and Trudgill, 1985; Di Prima et al., 2018; Llorens et al., 2021). Other authors have also reported similar values. For example, Schwärzel et al. (2012), using dye experiments and direct observations of dye-stained cross-sectional patterns in a beech forest in Germany, estimated flow velocities consistent with macropore flow exceeding 800 mm h^{-1}. The authors observed that stemflow and root-driven preferential flow beneath beech trees triggered rapid subsurface flow, bypassing much of the soil matrix. Di Prima et al. (2023) reported values of preferential flow velocity ranging from 1.9×10^3 to 1.2×10^4 mm h^{-1} through repeated GPR surveys and stemflow simulations conducted on a forested hillslope near Valencia, Spain.

4.3. Considerations on overland flow collection across two spatial scales

The assumptions discussed in Section 3.5 enabled the estimation of the steady-state stemflow infiltration rate at the plot scale (Table 2, Procedure 2, Step 6), yielding a $SIR_{ST\text{-}PLOT}$ value of 1065.1 mm h^{-1} (Figure 5b), which closely matches the mean steady-state stemflow infiltration rate estimated for individual trees ($mean(SIR_{ST\text{-}TREE})$ = 1031.9 mm h^{-1}) (Figure 5a). The similarity between the mean $SIR_{ST\text{-}TREE}$ value and $SIR_{ST\text{-}PLOT}$ suggests that similar processes occurred at both spatial scales. To understand this relationship, it is important to consider that overland flow volumes were collected at two different locations: beneath the plot during the second day of the plot-scale simulation and near the trees during the tree-scale stemflow simulations. Much of the generated overland flow therefore did not infiltrate near the stem bases and instead likely flowed for several meters across the soil surface due to the steep local slope (30°). This process is likely to become substantial during intense

storms, as concentrated rainfall at the stem bases and channelization caused by microtopography can activate erosion processes (Herwitz, 1986; Keen et al., 2010). A corollary implication from our experiments is that directly estimating stemflow infiltration areas based on observed wetting patterns on the soil surface is inadequate for accurately calculating infiltration rates. Nonetheless, this approach is commonly applied on level forest soils (e.g., Llorens et al., 2021). More accurate strategies involve estimating stemflow infiltration rates for cross-sectional dye-stained areas observed from trenches excavated downslope of the trees (e.g., Schwärzel et al., 2012). However, these approaches are destructive and require significant effort to quantify wetting patterns, as accurately observing deep dye patterns requires sectioning the soil along various vertical or horizontal planes (Di Prima et al., 2022). Before quantifying fluxes, it is essential to have a clear understanding of the flow pathways.

In this investigation, we used ERT imaging to visualize deep cross-sections and validating the selected criterion for determining infiltration areas, which at the surface was equaled to tree basal areas, with buffer areas $L_{BUFFER} = r_B \times (\sqrt{2}–1)$. More specifically, the monitoring of the resistivity changes allowed us to define the cross-sectional area activated by the infiltration for the successive conceptual and numerical models. Both stemflow and throughfall simulations only activated part of the cuboid cross section. These cross-sections were estimated to be around 0.5 m^2 for both stemflow and throughfall simulations, with a tendency to have central infiltration associated to the stemflow and more extended infiltration during the throughfall simulations. The similarity of the flow pathways of the two stemflow simulations suggest that these preferential pathways and thus cross-sections tend to remain the same when changing the water content.

4.4. Overall hydraulic functioning of the roots-soil system at the 100 m^2 spatial scale

In Section 3.6, we presented the separate parameterization of the two soil regions through numerical inversions, using infiltration data from the artificial throughfall and stemflow events conducted on the first day. The matrix region between tree stems had a K_s value of 217.5 mm h^{-1}, consistent with the values derived from infiltrometer data using the analytical fractional wettability infiltration model (Table 3). This finding supports our hypothesis that the infiltrometer tests provided K_s estimates that accurately represent the area between tree stems and further validates the reliability of the adopted analytical model (Eq. (2)). For the fast-flow region beneath the tree stems, we obtained K_s values ranging from 404.2 to 1,636.5 mm h^{-1}, with a mean value of 1,032.9 mm h^{-1}, which was 4.7 times higher than the K_s value representative of the matrix region between the stems, clearly demonstrating the double-permeability characteristics of the investigated forested soil.

The water content within the soil profile at 0.875 hours and 1.75 hours from the start of the 2D simulation conducted on Tree 5 is shown in the Figure in Appendix F. The water content distribution exhibited similar patterns to those observed in the ERT inverted 3D model (Figure 6a). This result provides confidence in the soil parameters obtained through the inversion procedure, which were subsequently implemented in the 2D simulation using a double-permeability approach. Consistent with ERT imaging and despite the high local slope, infiltration was primarily vertical and occurred near the stem. This can be attributed to the absence of a restrictive layer in the soil profile (Schwärzel et al., 2012), as observed during trench excavation, and the high infiltrability of the deeper horizons measured by infiltrometers (see Section 3.1), and, notably, the lack of capillarity in the macropores that make up the root system.

The final objective of these numerical simulations was to parameterize the soil-root system at the 100 m^2 spatial scale, accounting for the partitioning of rainfall into throughfall and stemflow and

quantifying the contribution of trees to subsurface water flow. To achieve this, the overall hydraulic functioning of the system was characterized by numerically inverting the infiltration data from the artificial throughfall and stemflow events conducted simultaneously on the second day (12:25 AM–6:05 PM). In accordance with the considerations discussed in Section 3.5, we estimated the fraction of surface flow infiltrating at the tree bases by subtracting the total applied throughfall from the measured total infiltration, yielding a value of 35.2% (flowchart in Appendix C). This resulted in a cumulative infiltration curve for the matrix region comparable to that of the first day of the artificial throughfall event (Figure 7b versus 7a), with a volume representing 64.8% of the total infiltration in both regions and steady infiltration rates of 7.98 mm h^{-1} in both cases (Figure 7d versus 7c), closely matching the intensity of the throughfall rainfall component. The inversion yielded an optimized K_s value of 1,047.4 mm h^{-1}, aligning with values obtained from the individual stemflow events. The volumetric fraction w (−) of the pore space occupied by the fast-flow region was 0.06, indicating that 6% of the total system porosity was occupied by macropores located beneath the stems. This value is consistent with those reported in many dual-permeability applications, as the fast-flow region generally occupies a very small fraction of the soil porosity, e.g., < 0.10 (Bouma et al., 1977; Dusek et al., 2012).

4.5. Insights into lateral subsurface flow from GPR monitoring at the plot scale

The comparison between the two GPR surveys, conducted before and after the two days of experiments, revealed an increase in amplitude signals at a depth of approximately 1–2.5 m, indicative of soil imbibition (Figure 8a). These findings suggest the activation of lateral subsurface flow, consistent with previous hypotheses proposed for the Lecciona site (Fabiani et al., 2024). A schematic representation of the observed subsurface lateral flow at the experimental plot is presented in Figure 8b. While numerical inversions enabled us to characterize flow dynamics at both the single-tree and plot-scale (100 m^2), the identification of a vertical fast-flow region activated by concentrated stemflow infiltration suggests the initiation of lateral subsurface flow at greater depths. This dynamic align with the conceptual model proposed by Germer (2013), which suggests that high-intensity water input from stemflow can result in one of three possible subsurface processes: (i) Horton overland flow, (ii) subsurface saturation above a restrictive soil layer, or (iii) rapid deep percolation along tree roots, leading to the formation of a perched water table at the soil–bedrock interface. Field observations from our artificial stemflow events and geophysical findings, indicate that the first two processes are of limited relevance, providing strong evidence that the third process is the dominant one. According to Macchioli Grande et al. (2024), the combination of steep topography and subsurface characteristics at the Lecciona site may facilitate lateral fast subsurface flow, which significantly influences groundwater recharge at the foot of the hillslope. This hypothesis is further explored in the following section.

4.6. Insights from piezometer data at the hillslope scale

At the Lecciona site, the presence of both vertical (stemflow-induced) and lateral (topography- and lithology-driven) fast-flow pathways is expected to result in rapid groundwater level fluctuations in response to intense rainfall, indicating the activation of fast-flow dynamics along the hillslope (Pirastru et al., 2022). To validate this hypothesis, we referred to the piezometer data published by Macchioli Grande et al. (2024). We selected three events from their work: May 1, 2021; July 6, 2021; and September 16, 2021, all resulting in a rise in groundwater levels (Figure 9). The maximum recorded rainfall intensities were 10.6 mm h^{-1} for the first event, 83.0 mm h^{-1} for the second event and 83.7 mm h^{-1} for the third (Δt = 10 min). Specifically, we considered the elapsed time from the start of the precipitation event to the initial response of the piezometer level. During these events, the

groundwater level response to precipitation varied depending on the location of the well, along with the amount and intensity of precipitation. The most reactive well was GW3, where we observed the fastest groundwater level increases during the three events considered. These increases occurred within just 5 minutes for the event on July 6, 35 minutes for the event on September 26, and 1 hour and 5 minutes for the event on May 1. During the event on July 6, the extreme recorded rainfall intensities, with 23.8 mm of precipitation in the first 30 minutes, caused a sudden and significant increase in the groundwater level. During the other two events, the responses were of lesser magnitude and slower, as a consequence of less intense and more prolonged precipitations. Compared to GW3, the responses at GW1, also located in the riparian zone, were delayed for all three precipitation events. The increases occurred within 50 minutes for the event on July 6, 1 hour and 35 minutes for the event on September 26, and 1 hour and 45 minutes for the event on May 1. During the event on July 6, the extreme recorded rainfall intensities caused at this location only a slightly increase of ground water level. Macchioli Grande et al. (2024) attributed this different behavior to seasonality in the GW1 response, noting that it was almost unresponsive to even the heaviest precipitation events when these followed periods of little or no rainfall. The responses to the three events at these two wells in the riparian zone are consistent with the results reported by Macchioli Grande et al. (2024), with the groundwater level at GW3 being the most reactive, exhibiting a flashy response to precipitation. During the event on July 6, GW2, located at the foot of the hillslope, responded immediately within the first 5 minutes of rainfall onset. In contrast, more delayed responses were observed for the other two events: within 50 minutes for the event on September 26 and within 3 hours and 15 minutes for the event on May 1. In conclusion, the presence of fast flow, leading to a rapid response in groundwater levels, is clearly identified and aligns with recharge occurring through the stem and root systems.

5. Summary and conclusions

In this study, we demonstrated that the forest soil in the "Re della Pietra" catchment exhibits dual-domain behavior, characterized by contrasting infiltration dynamics between the matrix and fast-flow regions in response to stemflow infiltration at the tree bases and throughfall infiltration between tree stems. Infiltrometer tests revealed that the soil between tree stems has lower infiltrability than that at the tree base, with K_s ranging from 177.8 to 237.4 mm h^{-1}. The classification of cumulative infiltration curves into distinct shapes highlighted the influence of fractional wettability phenomena, wherein an uneven distribution of water-repellent materials at the soil surface initially delays infiltration under dry conditions. Artificial throughfall events confirmed that, although the applied rainfall intensity was significantly lower than the soil's infiltration capacity, the presence of water-repellent fractions temporarily impeded infiltration until the soil moisture increased and a steady state was reached. In contrast, artificial stemflow events—conducted at rates exceeding the local infiltration capacity—indicated that water rapidly infiltrates at the base of tree stems through macropores and fractures. This response was evidenced by high steady-state infiltration rates, with mean values around 1031.9 mm h^{-1}, highlighting the critical role of macropores and fractures in facilitating fast-flow and infiltration.

Numerical inversions with HYDRUS-1D, which yielded consistent hydraulic parameters for both the matrix and fast-flow regions. The dual-permeability modeling approach revealed that, despite the fast-flow region constituting only about 6% of the total porosity, its hydraulic conductivity was significantly enhanced relative to the surrounding soil matrix. Geophysical techniques, such as ERT and GPR, provided complementary evidence by visualizing the subsurface distribution of water. ERT results identified concentrated vertical wetting beneath tree stems, while GPR surveys detected lateral subsurface flow at greater depths, indicative of complex flow processes activated under intense

rainfall conditions. The 2D simulation of flow around the tree further enhanced confidence in the soil parameters derived from the inversion procedure, providing a reliable reproduction of subsurface dynamics that closely matched those indirectly observed through ERT. Piezometer data allowed to identify fast-flow pathways at the hillslope spatial scale by detecting sudden rises in the water table. The observed reaction times aligned with the proposed conceptual model presented in Figure 8c, which depicts two interconnected fast-flow regions: a vertical region and a deeper lateral region. The vertical fast-flow region, triggered by concentrated stemflow infiltration, and its continuity with a deeper lateral fast-flow region provided a plausible explanation for the rapid fluctuations in groundwater levels observed during intense rainfall events. Additionally, these dynamics were consistent with our geophysical observations (Figures 6 and 8) and aligned with Germer's (2013) conceptual model.

In conclusion, this study underscores the importance of a multi-approach and multi-scale strategy to delineate the complex hydraulic functioning of forested hillslopes. Furthermore, it emphasizes the necessity of investigating each process at the appropriate spatial scale, as certain processes may become undetectable or irrelevant when observed at a smaller or larger scale. For example, modelers often criticize field infiltrometer measurements and laboratory K_s data for their inability to be upscaled from point measurements. However, this work highlights the crucial role of point-scale K_s measurements in characterizing and parameterizing a part of more complex systems consisting of multiple flow regions. At the same time, more labor-intensive protocols need to be implemented to account for the role of trees in subsurface water dynamics. For example, coupling stemflow and throughfall artificial experiments allowed us to evaluate the role of rainfall partitioning in the hydraulic response of the forested hillslope to precipitation. This protocol can be useful in developing detailed conceptual models, which can then be integrated into hillslope hydrological models or, on a larger scale, in semi-distributed catchment models.

Funding

This work was supported by the project "Unravelling interactions between WATER and carbon cycles during drought and their impact on water resources and forest and grassland ecosySTEMs in the Mediterranean climate – WATERSTEM" (call PRIN 2020, code: 20202WF53Z), funded by the Italian Ministry of University and Research (MUR).

SDP and FG also thank the support by the project: "Methodological proposal for the Individuation of protection forests through LEgislation, geohazard assessment Toolsand Ontology, MILETO" (PRIN 2022 PNRR; code: P2022587PM), funded by the European Union—Next Generation EU.

DP and IM also thank the support by the following projects: "WATer mixing in the critical ZONe: observations and predictions under environmental changes – WATZON" (call PRIN 2017, code: 2017SL7ABC), funded by the Italian Ministry of University and Research (MUR); "Carbon and water cycles interactions during drought and their impact on WAter and ForEst Resources in the Mediterranean region -WAFER" funded by the Italian National research Council (Consiglio Nazionale delle Ricerche – CNR); "Hydrological controls on carbonate-mediated CO2 consumptions – HYDRO4C (call PRIN 2022, code: 2022PFNNRS) funded by the European Union, Next Generation EU; and "Space It Up!" (call ASI n. 687/2022 of 26 July 2022, contract ASI N. 2024-5-E.0, master code: 685 I53D24000060005, WP 7.6), funded by the Italian Space Agency (ASI) and the Italian Ministry of686 University and Research (MUR).

LP and GC also thank the support by the following projects: RETURN Extended Partnership and received funding from the European Union Next-GenerationEU (National Recovery and Resilience Plan – NRRP, Mission 4, Component 2, Investment 1.3 – D.D. 1243 2/8/2022, PE0000005); Geosciences for Sustainable Development project (Budget Ministero dell'Università e della Ricerca Dipartimenti di Eccellenza 2023-2027 C93C23002690001).

Acknowledgement

The authors thank the local Forest Service (Unione Comuni Valdarno Valdisieve) for their logistical support in managing the Re della Pietra experimental catchment. The authors also thank Andrea Dani, Matteo Verdone, Clara Rhode, Federico Preti, Giulia Zuecco, Chiara Marchina for their help in the field. The authors also thank Alberto Cogliati and Viola Cioffi for their contribution to assembling the ERT components in the laboratory. A special thanks also goes to the *Colonnello* for his contribution in keeping our stomachs full and our spirits lifted.

Credit authorship contribution statement

- Simone Di Prima: Conceptualization, Methodology, Investigation, Formal analysis, Validation, Visualization, Writing – original draft (entire manuscript except for Sections 2.4, 2.5, and 3.4), Writing - Review & Editing, Funding acquisition.
- Gersende Fernandes: Writing – original draft (Section 2.5), Writing - Review & Editing.
- Maria Burguet: Investigation, Writing - Review & Editing.
- Maria Paz Salazar: Investigation, Writing - Review & Editing.
- Elisa Marras: Investigation, Writing - Review & Editing.
- Ilenia Murgia: Investigation, Writing - Review & Editing.
- Konstantinos Kaffas: Investigation, Writing - Review & Editing.
- Luca Peruzzo: Investigation, Formal analysis, Validation, Visualization, Writing – original draft (Sections: 2.4, 3.4), Writing - Review & Editing, Funding acquisition.
- Ryan D. Stewart: Writing - Review & Editing.
- Majdi R. Abou Najm: Writing - Review & Editing.
- Alessandro Comegna: Writing - Review & Editing.
- Laurent Lassabatere: Writing - Review & Editing, Resources.
- Giorgio Cassiani: Investigation, Writing - Review & Editing, Funding acquisition.
- Daniele Penna: Writing - Review & Editing, Funding acquisition.
- Christian Massari: Writing - Review & Editing, Funding acquisition.
- Filippo Giadrossich: Methodology, Investigation, Writing - Review & Editing, Funding acquisition.

Declaration of Competing Interest

The authors declare that they have no known competing financial interests or personal relationships that could have appeared to influence the work reported in this paper.

References

Abou Najm, M.R., Stewart, R.D., Di Prima, S., Lassabatere, L., 2021. A simple correction term to model infiltration in water-repellent soils. Water Resour. Res. 57. https://doi.org/10.1029/2020WR028539

Amendola, U., Perri, F., Critelli, S., Monaco, P., Cirilli, S., Trecci, T., Rettori, R., 2016. Composition and provenance of the Macigno Formation (Late Oligocene–Early Miocene) in

the Trasimeno Lake area (northern Apennines). Mar. Pet. Geol. 69, 146–167. https://doi.org/10.1016/j.marpetgeo.2015.10.019
Angulo-Jaramillo, R., Bagarello, V., Di Prima, S., Gosset, A., Iovino, M., Lassabatere, L., 2019. Beerkan Estimation of Soil Transfer parameters (BEST) across soils and scales. J. Hydrol. 576, 239–261. https://doi.org/10.1016/j.jhydrol.2019.06.007
Angulo-Jaramillo, R., Bagarello, V., Iovino, M., Lassabatere, L., 2016. Saturated Soil Hydraulic Conductivity, in: Infiltration Measurements for Soil Hydraulic Characterization. Springer International Publishing, pp. 43–180. https://doi.org/10.1007/978-3-319-31788-5_2
Bachmann, J., Krueger, J., Goebel, M.-O., Heinze, S., 2016. Occurrence and spatial pattern of water repellency in a beech forest subsoil. J. Hydrol. Hydromech. 64, 100–110. https://doi.org/10.1515/johh-2016-0005
Basset, C., Abou Najm, M., Angulo-Jaramillo, R., Bagarello, V., Ghanbarian, B., Di Prima, S., Iovino, M., Lassabatère, L., Stewart, R., 2025. Review of conceptual and empirical approaches to characterize infiltration. Vadose Zone J. 24, e20393. https://doi.org/10.1002/vzj2.20393
Binley, A., Hubbard, S.S., Huisman, J.A., Revil, A., Robinson, D.A., Singha, K., Slater, L.D., 2015. The emergence of hydrogeophysics for improved understanding of subsurface processes over multiple scales. Water Resour. Res. 51, 3837–3866. https://doi.org/10.1002/2015WR017016
Bouma, J., Jongerius, A., Boersma, O., Jager, A., Schoonderbeek, D., 1977. The function of different types of macropores during saturated flow through four swelling soil horizons. Soil Sci. Soc. Am. J. 41, 945–950.
Buczko, U., Bens, O., Hüttl, R.F., 2005. Variability of soil water repellency in sandy forest soils with different stand structure under Scots pine (Pinus sylvestris) and beech (Fagus sylvatica). Geoderma 126, 317–336. https://doi.org/10.1016/j.geoderma.2004.10.003
Cassiani, G., Boaga, J., Rossi, M., Putti, M., Fadda, G., Majone, B., Bellin, A., 2016. Soil–plant interaction monitoring: Small scale example of an apple orchard in Trentino, North-Eastern Italy. Sci. Total Environ., Special Issue on Climate Change, Water and Security in the Mediterranean 543, 851–861. https://doi.org/10.1016/j.scitotenv.2015.03.113
Cassiani, G., Boaga, J., Vanella, D., Perri, M.T., Consoli, S., 2015. Monitoring and modelling of soil–plant interactions: the joint use of ERT, sap flow and eddy covariance data to characterize the volume of an orange tree root zone. Hydrol. Earth Syst. Sci. 19, 2213–2225. https://doi.org/10.5194/hess-19-2213-2015
Crabtree, R.W., Trudgill, S.T., 1985. Hillslope hydrochemistry and stream response on a wooded, permeable bedrock: The role of stemflow. J. Hydrol. 80, 161–178. https://doi.org/10.1016/0022-1694(85)90079-4
DeBano, L.F., 2000. Water repellency in soils: a historical overview. J. Hydrol. 231, 4–32.
Dekker, L.W., Ritsema, C.J., 1994. How water moves in a water repellent sandy soil: 1. Potential and actual water repellency. Water Resour. Res. 30, 2507–2517. https://doi.org/10.1029/94WR00749
Di Prima, S., 2015. Automated single ring infiltrometer with a low-cost microcontroller circuit. Comput. Electron. Agric. 118, 390–395. https://doi.org/10.1016/j.compag.2015.09.022
Di Prima, S., Fernandes, G., Marras, E., Giadrossich, F., Stewart, R.D., Abou Najm, M.R., Winiarski, T., Mourier, B., Angulo-Jaramillo, R., Comegna, A., del Campo, A., Lassabatere, L., 2023. Evaluating subsurface flow connectivity in a pine-covered hillslope with stemflow infiltration and ground-penetrating radar surveys. J. Hydrol. 620, 129527. https://doi.org/10.1016/j.jhydrol.2023.129527
Di Prima, S., Giannini, V., Ribeiro Roder, L., Giadrossich, F., Lassabatere, L., Stewart, R.D., Abou Najm, M.R., Longo, V., Campus, S., Winiarski, T., Angulo-Jaramillo, R., del Campo, A., Capello, G., Biddoccu, M., Roggero, P.P., Pirastru, M., 2022. Coupling time-lapse ground penetrating radar surveys and infiltration experiments to characterize two types of non-

931 uniform flow. Sci. Total Environ. 806, 150410.
932 https://doi.org/10.1016/j.scitotenv.2021.150410
933 Di Prima, S., Lassabatere, L., Bagarello, V., Iovino, M., Angulo-Jaramillo, R., 2016. Testing a new
934 automated single ring infiltrometer for Beerkan infiltration experiments. Geoderma 262, 20–
935 34. https://doi.org/10.1016/j.geoderma.2015.08.006
936 Di Prima, S., Marrosu, R., Lassabatere, L., Angulo-Jaramillo, R., Pirastru, M., 2018. In situ
937 characterization of preferential flow by combining plot- and point-scale infiltration
938 experiments on a hillslope. J. Hydrol. 563, 633–642.
939 https://doi.org/10.1016/j.jhydrol.2018.06.033
940 Di Prima, S., Stewart, R.D., Abou Najm, M.R., Ribeiro Roder, L., Giadrossich, F., Campus, S.,
941 Angulo-Jaramillo, R., Yilmaz, D., Roggero, P.P., Pirastru, M., Lassabatere, L., 2021. BEST-
942 WR: An adapted algorithm for the hydraulic characterization of hydrophilic and water-
943 repellent soils. J. Hydrol. 603, 126936. https://doi.org/10.1016/j.jhydrol.2021.126936
944 Di Prima, S., Stewart, R.D., Abou Najm, M.R., Yilmaz, D., Comegna, A., Lassabatere, L., 2025.
945 Modeling water infiltration into soil under fractional wettability conditions. J. Hydrol. 647,
946 132309. https://doi.org/10.1016/j.jhydrol.2024.132309
947 Doerr, S.H., Shakesby, R.A., Walsh, R.P.D., 2000. Soil water repellency: its causes, characteristics
948 and hydro-geomorphological significance. Earth-Sci. Rev. 51, 33–65.
949 Doerr, S.H., Thomas, A.D., 2000. The role of soil moisture in controlling water repellency: new
950 evidence from forest soils in Portugal. J. Hydrol. 231–232, 134–147.
951 https://doi.org/10.1016/S0022-1694(00)00190-6
952 Durocher, M.G., 1990. Monitoring spatial variability of forest interception. Hydrol. Process. 4, 215–
953 229. https://doi.org/10.1002/hyp.3360040303
954 Dusek, J., Vogel, T., Dohnal, M., Gerke, H.H., 2012. Combining dual-continuum approach with
955 diffusion wave model to include a preferential flow component in hillslope scale modeling
956 of shallow subsurface runoff. Adv. Water Resour. 44, 113–125.
957 https://doi.org/10.1016/j.advwatres.2012.05.006
958 Fabiani, G., Klaus, J., Penna, D., 2024. The influence of hillslope topography on beech water use: a
959 comparative study in two different climates. Hydrol. Earth Syst. Sci. 28, 2683–2703.
960 https://doi.org/10.5194/hess-28-2683-2024
961 Fan, B., Liu, X., Zhu, Q., Qin, G., Li, J., Lin, H., Guo, L., 2020. Exploring the interplay between
962 infiltration dynamics and Critical Zone structures with multiscale geophysical imaging: A
963 review. Geoderma 374, 114431. https://doi.org/10.1016/j.geoderma.2020.114431
964 Gerke, H.H., 2006. Preferential flow descriptions for structured soils. J. Plant Nutr. Soil Sci. 169,
965 382–400. https://doi.org/10.1002/jpln.200521955
966 Gerke, H.H., Genuchten, M.T. van, 1993. A dual-porosity model for simulating the preferential
967 movement of water and solutes in structured porous media. Water Resour. Res. 29, 305–319.
968 https://doi.org/10.1029/92WR02339
969 Germer, S., 2013. Development of near-surface perched water tables during natural and artificial
970 stemflow generation by babassu palms. J. Hydrol. 507, 262–272.
971 https://doi.org/10.1016/j.jhydrol.2013.10.026
972 Geuzaine, C., Remacle, J.-F., 2009. Gmsh: A 3-D finite element mesh generator with built-in pre-
973 and post-processing facilities. Int. J. Numer. Methods Eng. 79, 1309–1331.
974 https://doi.org/10.1002/nme.2579
975 Guo, L., Mount, G.J., Hudson, S., Lin, H., Levia, D., 2020. Pairing geophysical techniques
976 improves understanding of the near-surface Critical Zone: Visualization of preferential
977 routing of stemflow along coarse roots. Geoderma 357, 113953.
978 https://doi.org/10.1016/j.geoderma.2019.113953
979 Haverkamp, R., Ross, P.J., Smettem, K.R.J., Parlange, J.Y., 1994. Three-dimensional analysis of
980 infiltration from the disc infiltrometer: 2. Physically based infiltration equation. Water
981 Resour. Res. 30, 2931–2935. https://doi.org/10.1029/94WR01788

Hemr, O., Vichta, T., Brychtová, M., Kupec, P., Žižlavská, N., Tomášová, G., Deutscher, J., 2023. Stemflow infiltration hotspots near-tree stems along a soil depth gradient in a mixed oak–beech forest. Eur. J. For. Res. https://doi.org/10.1007/s10342-023-01592-7

Herwitz, S.R., 1986. Infiltration-excess caused by Stemflow in a cyclone-prone tropical rainforest. Earth Surf. Process. Landf. 11, 401–412. https://doi.org/10.1002/esp.3290110406

Ireson, A.M., Butler, A.P., 2011. Controls on preferential recharge to Chalk aquifers. J. Hydrol. 398, 109–123. https://doi.org/10.1016/j.jhydrol.2010.12.015

Jackisch, C., Germer, K., Graeff, T., Andrä, I., Schulz, K., Schiedung, M., Haller-Jans, J., Schneider, J., Jaquemotte, J., Helmer, P., Lotz, L., Bauer, A., Hahn, I., Šanda, M., Kumpan, M., Dorner, J., de Rooij, G., Wessel-Bothe, S., Kottmann, L., Schittenhelm, S., Durner, W., 2020. Soil moisture and matric potential – an open field comparison of sensor systems. Earth Syst. Sci. Data 12, 683–697. https://doi.org/10.5194/essd-12-683-2020

Johnson, M.S., Lehmann, J., 2006. Double-funneling of trees: Stemflow and root-induced preferential flow. Écoscience 13, 324–333. https://doi.org/10.2980/i1195-6860-13-3-324.1

Keen, B., Cox, J., Morris, S., Dalby, T., 2010. Stemflow runoff contributes to soil erosion at the base of macadamia trees.

Krueger, J., Böttcher, J., Schmunk, C., Bachmann, J., 2016. Soil water repellency and chemical soil properties in a beech forest soil — Spatial variability and interrelations. Geoderma 271, 50–62. https://doi.org/10.1016/j.geoderma.2016.02.013

Lassabatere, L., Angulo-Jaramillo, R., Soria Ugalde, J.M., Cuenca, R., Braud, I., Haverkamp, R., 2006. Beerkan estimation of soil transfer parameters through infiltration experiments—BEST. Soil Sci. Soc. Am. J. 70, 521. https://doi.org/10.2136/sssaj2005.0026

Lee, L.J.E., Lawrence, D.S.L., Price, M., 2006. Analysis of water-level response to rainfall and implications for recharge pathways in the Chalk aquifer, SE England. J. Hydrol. 330, 604–620. https://doi.org/10.1016/j.jhydrol.2006.04.025

Levia, D.F., Frost, E.E., 2003. A review and evaluation of stemflow literature in the hydrologic and biogeochemical cycles of forested and agricultural ecosystems. J. Hydrol. 274, 1–29. https://doi.org/10.1016/S0022-1694(02)00399-2

Liang, W.-L., 2020. Effects of Stemflow on Soil Water Dynamics in Forest Stands, in: Levia, D.F., Carlyle-Moses, D.E., Iida, S., Michalzik, B., Nanko, K., Tischer, A. (Eds.), Forest-Water Interactions, Ecological Studies. Springer International Publishing, Cham, pp. 349–370. https://doi.org/10.1007/978-3-030-26086-6_15

Liang, W.-L., Kosugi, K., Mizuyama, T., 2009. A three-dimensional model of the effect of stemflow on soil water dynamics around a tree on a hillslope. J. Hydrol. 366, 62–75. https://doi.org/10.1016/j.jhydrol.2008.12.009

Llorens, P., Domingo, F., 2007. Rainfall partitioning by vegetation under Mediterranean conditions. A review of studies in Europe. J. Hydrol. 335, 37–54. https://doi.org/10.1016/j.jhydrol.2006.10.032

Llorens, P., Latron, J., Carlyle-Moses, D.E., Näthe, K., Chang, J.L., Nanko, K., Iida, S., Levia, D.F., 2021. Stemflow Infiltration Areas Into Forest Soils Around American Beech (Fagus grandifolia Ehrh.) Trees. Ecohydrology n/a, e2369. https://doi.org/10.1002/eco.2369

Macchioli Grande, M., Kaffas, K., Verdone, M., Borga, M., Cocozza, C., Dani, A., Errico, A., Fabiani, G., Gourdol, L., Klaus, J., Manca di Villahermosa, F.S., Massari, C., Murgia, I., Pfister, L., Preti, F., Segura, C., Tailliez, C., Trucchi, P., Zuecco, G., Penna, D., 2024. Seasonal meteorological forcing controls runoff generation at multiple scales in a Mediterranean forested mountain catchment. J. Hydrol. 639, 131642. https://doi.org/10.1016/j.jhydrol.2024.131642

Mary, B., Peruzzo, L., Boaga, J., Cenni, N., Schmutz, M., Wu, Y., Hubbard, S.S., Cassiani, G., 2020. Time-lapse monitoring of root water uptake using electrical resistivity tomography and mise-à-la-masse: a vineyard infiltration experiment. SOIL 6, 95–114. https://doi.org/10.5194/soil-6-95-2020

Mary, B., Peruzzo, L., Boaga, J., Schmutz, M., Wu, Y., Hubbard, S.S., Cassiani, G., 2018. Small-scale characterization of vine plant root water uptake via 3-D electrical resistivity tomography and mise-à-la-masse method. Hydrol. Earth Syst. Sci. 22, 5427–5444. https://doi.org/10.5194/hess-22-5427-2018

Neave, M., Abrahams, A.D., 2002. Vegetation influences on water yields from grassland and shrubland ecosystems in the Chihuahuan Desert. Earth Surf. Process. Landf. 27, 1011–1020. https://doi.org/10.1002/esp.389

Nikodem, A., Kodešová, R., Drábek, O., Bubeníčková, L., Borůvka, L., Pavlů, L., Tejnecký, V., 2010. A Numerical Study of the Impact of Precipitation Redistribution in a Beech Forest Canopy on Water and Aluminum Transport in a Podzol. Vadose Zone J. 9, 238–251. https://doi.org/10.2136/vzj2009.0083

Pachepsky, Y., Hill, R.L., 2017. Scale and scaling in soils. Geoderma, Structure and function of soil and soil cover in a changing world: characterization and scaling 287, 4–30. https://doi.org/10.1016/j.geoderma.2016.08.017

Pachepsky, Y., Karahan, G., 2022. On shapes of cumulative infiltration curves. Geoderma 412, 115715. https://doi.org/10.1016/j.geoderma.2022.115715

Peruzzo, L., Chou, C., Hubbard, S.S., Brodie, E., Uhlemann, S., Dafflon, B., Wielandt, S., Mary, B., Cassiani, G., Morales, A., Wu, Y., 2024. Outdoor mesoscale fabricated ecosystems: Rationale, design, and application to evapotranspiration. Sci. Total Environ. 957, 177565. https://doi.org/10.1016/j.scitotenv.2024.177565

Peruzzo, L., Chou, C., Wu, Y., Schmutz, M., Mary, B., Wagner, F.M., Petrov, P., Newman, G., Blancaflor, E.B., Liu, X., Ma, X., Hubbard, S., 2020. Imaging of plant current pathways for non-invasive root Phenotyping using a newly developed electrical current source density approach. Plant Soil 450, 567–584. https://doi.org/10.1007/s11104-020-04529-w

Pirastru, M., Iovino, M., Marrosu, R., Di Prima, S., Giadrossich, F., Awada, H., 2022. Large-scale lateral saturated soil hydraulic conductivity as a metric for the connectivity of subsurface flow paths at hillslope scale. Hydrol. Process. 36, e14649. https://doi.org/10.1002/hyp.14649

Rahmati, M., Weihermüller, L., Vanderborght, J., Pachepsky, Y.A., Mao, L., Sadeghi, S.H., Moosavi, N., Kheirfam, H., Montzka, C., Looy, K.V., Toth, B., Hazbavi, Z., Yamani, W.A., Albalasmeh, A.A., Alghzawi, M.Z., Angulo-Jaramillo, R., Antonino, A.C.D., Arampatzis, G., Armindo, R.A., Asadi, H., Bamutaze, Y., Batlle-Aguilar, J., Bechet, B., Becker, F., Blöschl, G., Bohne, K., Braud, I., Castellano, C., Cerdà, A., Chalhoub, M., Cichota, R., Císlerová, M., Clothier, B., Coquet, Y., Cornelis, W., Corradini, C., Coutinho, A.P., Oliveira, M.B. de, Macedo, J.R. de, Durães, M.F., Emami, H., Eskandari, I., Farajnia, A., Flammini, A., Fodor, N., Gharaibeh, M., Ghavimipanah, M.H., Ghezzehei, T.A., Giertz, S., Hatzigiannakis, E.G., Horn, R., Jiménez, J.J., Jacques, D., Keesstra, S.D., Kelishadi, H., Kiani-Harchegani, M., Kouselou, M., Kumar Jha, M., Lassabatere, L., Li, X., Liebig, M.A., Lichner, L., López, M.V., Machiwal, D., Mallants, D., Mallmann, M.S., Marques, O., De, J.D., Marshall, M.R., Mertens, J., Meunier, F., Mohammadi, M.H., Mohanty, B.P., Moncada, M.P., Montenegro, S., Morbidelli, R., Moret-Fernández, D., Moosavi, A.A., Mosaddeghi, M.R., Mousavi, S.B., Mozaffari, H., Nabiollahi, K., Neyshabouri, M.R., Ottoni, M.V., Filho, O., Benedicto, T., Rad, P., Reza, M., Panagopoulos, A., Peth, S., Peyneau, P.-E., Picciafuoco, T., Poesen, J., Pulido, M., Reinert, D.J., Reinsch, S., Rezaei, M., Roberts, F.P., Robinson, D., Rodrigo-Comino, J., Filho, R., Corrêa, O., Saito, T., Suganuma, H., Saltalippi, C., Sándor, R., Schütt, B., Seeger, M., Sepehrnia, N., Sharifi Moghaddam, E., Shukla, M., Shutaro, S., Sorando, R., Stanley, A.A., Strauss, P., Su, Z., Taghizadeh-Mehrjardi, R., Taguas, E., Teixeira, W.G., Vaezi, A.R., Vafakhah, M., Vogel, T., Vogeler, I., Votrubova, J., Werner, S., Winarski, T., Yilmaz, D., Young, M.H., Zacharias, S., Zeng, Y., Zhao, Y., Zhao, H., Vereecken, H., 2018. Development and Analysis of Soil Water Infiltration Global Database. Earth Syst. Sci. Data Discuss. 1–42. https://doi.org/10.5194/essd-10-1237-2018

Rücker, C., Günther, T., Wagner, F.M., 2017. pyGIMLi: An open-source library for modelling and inversion in geophysics. Comput. Geosci. 109, 106–123. https://doi.org/10.1016/j.cageo.2017.07.011

Sansoulet, J., Cabidoche, Y.-M., Cattan, P., Ruy, S., Šimůnek, J., 2008. Spatially Distributed Water Fluxes in an Andisol under Banana Plants: Experiments and Three-Dimensional Modeling. Vadose Zone J. 7, 819–829. https://doi.org/10.2136/vzj2007.0073

Schwärzel, K., Ebermann, S., Schalling, N., 2012. Evidence of double-funneling effect of beech trees by visualization of flow pathways using dye tracer. J. Hydrol. 470–471, 184–192. https://doi.org/10.1016/j.jhydrol.2012.08.048

Schwen, A., Zimmermann, M., Leitner, S., Woche, S.K., 2015. Soil Water Repellency and its Impact on Hydraulic Characteristics in a Beech Forest under Simulated Climate Change. Vadose Zone J. 14, vzj2015.06.0089. https://doi.org/10.2136/vzj2015.06.0089

Šimůnek, J., Brunetti, G., Genuchten, M.T. van, Šejna, M., 2024. The Family of HYDRUS Models, in: Oxford Research Encyclopedia of Environmental Science. https://doi.org/10.1093/acrefore/9780199389414.013.892

Spencer, S.A., van Meerveld, H.J. van, 2016. Double funnelling in a mature coastal British Columbia forest: spatial patterns of stemflow after infiltration. Hydrol. Process. 30, 4185–4201. https://doi.org/10.1002/hyp.10936

Staelens, J., De Schrijver, A., Verheyen, K., Verhoest, N.E.C., 2008. Rainfall partitioning into throughfall, stemflow, and interception within a single beech (Fagus sylvatica L.) canopy: influence of foliation, rain event characteristics, and meteorology. Hydrol. Process. 22, 33–45. https://doi.org/10.1002/hyp.6610

Taniguchi, M., Tsujimura, M., Tanaka, T., 1996. Significance of stemflow in groundwater recharge. 1: Evaluation of the stemflow contribution to recharge using a mass balance approach. Hydrol. Process. 10, 71–80. https://doi.org/10.1002/(SICI)1099-1085(199601)10:1<71::AID-HYP301>3.0.CO;2-Q

Tischer, A., Michalzik, B., Lotze, R., 2020. Nonuniform but highly preferential stemflow routing along bark surfaces and actual smaller infiltration areas than previously assumed: A case study on European beech (Fagus sylvatica L.) and sycamore maple (Acer pseudoplatanus L.). Ecohydrology 13, e2230. https://doi.org/10.1002/eco.2230

Uchida, T., Kosugi, K., Mizuyama, T., 2001. Effects of pipeflow on hydrological process and its relation to landslide: a review of pipeflow studies in forested headwater catchments. Hydrol. Process. 15, 2151–2174. https://doi.org/10.1002/hyp.281

van Genuchten, M.T., 1980. A closed-form equation for predicting the hydraulic conductivity of unsaturated soils. Soil Sci. Soc. Am. J. 44, 892–898. https://doi.org/sssaj1980.03615995004400050002x

Verdone, M., van Meerveld, I., Massari, C., Penna, D., 2025. Variability and temporal stability of throughfall along a hillslope. J. Hydrol. 647, 132294. https://doi.org/10.1016/j.jhydrol.2024.132294

Vereecken, H., Huisman, J.A., Bogena, H., Vanderborght, J., Vrugt, J.A., Hopmans, J.W., 2008. On the value of soil moisture measurements in vadose zone hydrology: A review. Water Resour. Res. 44. https://doi.org/10.1029/2008WR006829

Wessel, A.T., 1988. On using the effective contact angle and the water drop penetration time for classification of water repellency in dune soils. Earth Surf. Process. Landf. 13, 555–561. https://doi.org/10.1002/esp.3290130609

Wilkinson, P.B., Chambers, J.E., Meldrum, P.I., Kuras, O., Inauen, C.M., Swift, R.T., Curioni, G., Uhlemann, S., Graham, J., Atherton, N., 2022. Windowed 4D inversion for near real-time geoelectrical monitoring applications. Front. Earth Sci. 10. https://doi.org/10.3389/feart.2022.983603

1133

1134 Table 1. Characteristics of the artificial stemflow and throughfall events.

Day	Artificial event	Position	Hour start	Hour end	Duration	Duration	Stemflow rate	Volume	Crown projection area	Rainfall component height	Rainfall component intensity	Estimated incident rainfall height	Estimated incident rainfall intensity
			hh:mm	hh:mm	hh:mm	h	L min^{-1} $Tree^{-1}$	L	m^2	mm	mm h^{-1}	mm	mm h^{-1}
1	Stemflow	Trees 1-3	8:30	10:15	1:45	1.75	1.20	379	28.5	13.3	7.6	190.0	108.6
1	Stemflow	Tress 4-7	10:20	12:05	1:45	1.75	1.10	461	28.7	16.1	9.2	229.8	131.3
1	Throughfall	Plot	12:35	17:45	5:10	5.17		4156		41.6	8.0	58.5	11.3
2	Stemflow	Trees 1-3	8:30	10:15	1:45	1.75	1.18	373	28.5	13.1	7.5	187.0	106.9
2	Stemflow	Tress 4-7	10:20	12:05	1:45	1.75	1.11	465	28.7	16.2	9.3	231.8	132.5
2	Throughfall	Plot	12:25	18:05	5:40	5.67		4558		45.6	8.0	64.2	11.3
2	Stemflow	Trees 1-7	12:25	18:05	5:40	5.67	1.17	2783	57.2	48.7	8.6	695.6	122.7

1135

1136 Table 2. Procedures for estimating steady-state stemflow infiltration rates, SIR_{ST} (mm h^{-1}), at the tree and 100
1137 m^2 plot spatial scales.

PROCEDURE 1: estimation at the tree spatial scale				
Step	Description	Variable name	Measurement unit	Measurement method or Calculation
1	Supplied Stemflow Volume	SV_{TREE}	L	measured using flowmeter readings
2	Overland flow Volume	OV_{TREE}	L	collected using angular aluminum profiles
3	Stemflow Infiltration Volume	SIV_{TREE}	L	$SV_{TREE} - OV_{TREE}$
4	Duration of Steady stage	t_{ST}	h	evaluated from cumulative versus time plots (0.5 h)
5	Area at the Base of the Tree	ABT	m^2	measured on the field
6	Stemflow Infiltration Height	SIH_{TREE}	mm	SIV_{TREE} / ABT
7	Stemflow Infiltration Rate at Steady state	$SIR_{ST\text{-}TREE}$	mm h^{-1}	$SIH_{ST\text{-}TREE}$ / t_{ST}
PROCEDURE 2: estimation at the 100 m^2 plot spatial scale				
Step	Description	Variable name	Measurement unit	Measurement method or Calculation
1	Supplied Volume (Throughfall + Stemflow)	V_{PLOT}	L	measured using flowmeter readings
2	Throughfall Intensity	$I_{T\text{-}PLOT}$	mm h^{-1}	measured with rain gauges
3	Throughfall Volume	TV_{PLOT}	L	calculated using the measured $I_{T\text{-}PLOT}$ value
4	Overland flow Volume	OV_{PLOT}	L	collected using angular aluminum profiles
5	Infiltration Volume	IV_{PLOT}	L	$V_{PLOT} - OV_{PLOT}$
6	Stemflow Infiltration Volume	SIV_{PLOT}	L	$IV_{PLOT} - TV_{PLOT}$ (assuming that all the throughfall infiltrates)
7	Duration of Steady stage	t_{ST}	h	evaluated from cumulative versus time plots (2 h)
8	Sum of the Areas at the Bases of the Trees	$ABTs$	m^2	measured on the field
9	Stemflow Infiltration Height	SIH_{PLOT}	mm	SIV_{PLOT} / $ABTs$
10	Stemflow Infiltration Rate at Steady state	$SIR_{ST\text{-}PLOT}$	mm h^{-1}	$SIH_{ST\text{-}PLOT}$ / t_{ST}

1138

Table 3. Output of the fractional wettability infiltration model.

Variable	Depth [m]	Min	Max	Mean	Median	CV [%]
K_s [mm h^{-1}]	0	79.6	250.9	177.8 A†	204.6	44.4
	0.2	77.3	344.5	237.4 A	252.2	41.4
	0.4	179.7	337.5	224.6 A	196.1	29.1
S [mm h$^{-0.5}$]	0	80.4	108.5	91.1 A†	89.1	12.3
	0.2	54.9	135.8	98.4 A	116.4	37.8
	0.4	76.1	112.5	91.3 A	89.9	15.3
w_{FW} [–]	0	0.2	0.4	0.3 B†	0.4	30.5
	0.2	0.4	0.7	0.5 A	0.5	17.6
	0.4	0.5	0.6	0.5 A	0.5	12.2
α_{WR} [h^{-1}]	0	2.2	25.8	13.8	13.9 A††	76.6
	0.2	7.2	315.0	77.5	18.1 A	171.7
	0.4	9.3	2653.4	542.2	16.1 A	217.7

† For a given variable, means followed by the same letter were not significantly different according to the Tukey 's Honestly Significant Difference test ($P < 0.05$). †† For a given variable, medians followed by the same letter were not significantly different according to the Kruskal-Wallis test ($P < 0.05$).

1143 Table 4. Soil hydraulic parameters retrieved from the numerical simulations.

Simulation	Model	Matrix Flow Parameters					Fast Flow Parameters				
		θ_r ($m^3\ m^{-3}$)	θ_s ($m^3\ m^{-3}$)	α (mm^{-1})	n (-)	K_s ($mm\ h^{-1}$)	θ_r ($m^3\ m^{-3}$)	θ_s ($m^3\ m^{-3}$)	α (mm^{-1})	n (-)	K_s ($mm\ h^{-1}$)
Throughfall	Single Porosity	0.089†	0.523	0.0043†	1.442†	217.5†	NA	NA	NA	NA	NA
Stemflow Tree 1-2	Dual-Permeability	0.089	0.523	0.0043	1.442	217.5	0	0.740†	0.01	2	1128.2†
Stemflow Tree 3	Dual-Permeability	0.089	0.523	0.0043	1.442	217.5	0	0.764†	0.01	2	798.3†
Stemflow Tree 4	Dual-Permeability	0.089	0.523	0.0043	1.442	217.5	0	0.755†	0.01	2	1197.3†
Stemflow Tree 5	Dual-Permeability	0.089	0.523	0.0043	1.442	217.5	0	0.671†	0.01	2	404.2†
Stemflow Tree 6-7	Dual-Permeability	0.089	0.523	0.0043	1.442	217.5	0	0.730†	0.01	2	1636.6†
Throughfall + Stemflow	Dual-Permeability	0.089	0.523	0.0043	1.442	217.5	0	0.734	0.01	2	1047.4†

1144 † Fitted parameters.

1145

1146 Figure 1. Four spatial scales considered in this study for investigating subsurface water dynamics, with the
1147 techniques used to study each process at the corresponding spatial scale (in parentheses).

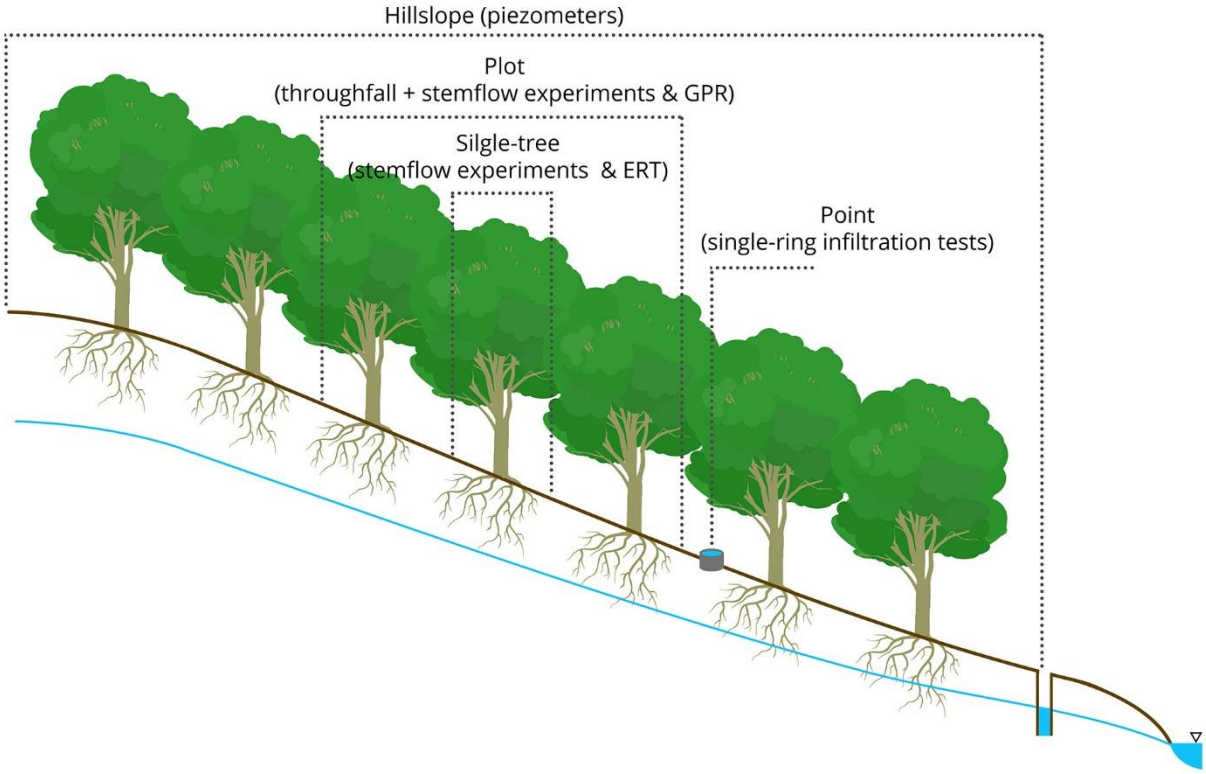

1148

1149

Figure 2. (a) Location of the Lecciona experimental site. (b) Experimental plot. (c) Setup of the water supply system used for the artificial stemflow and throughfall events

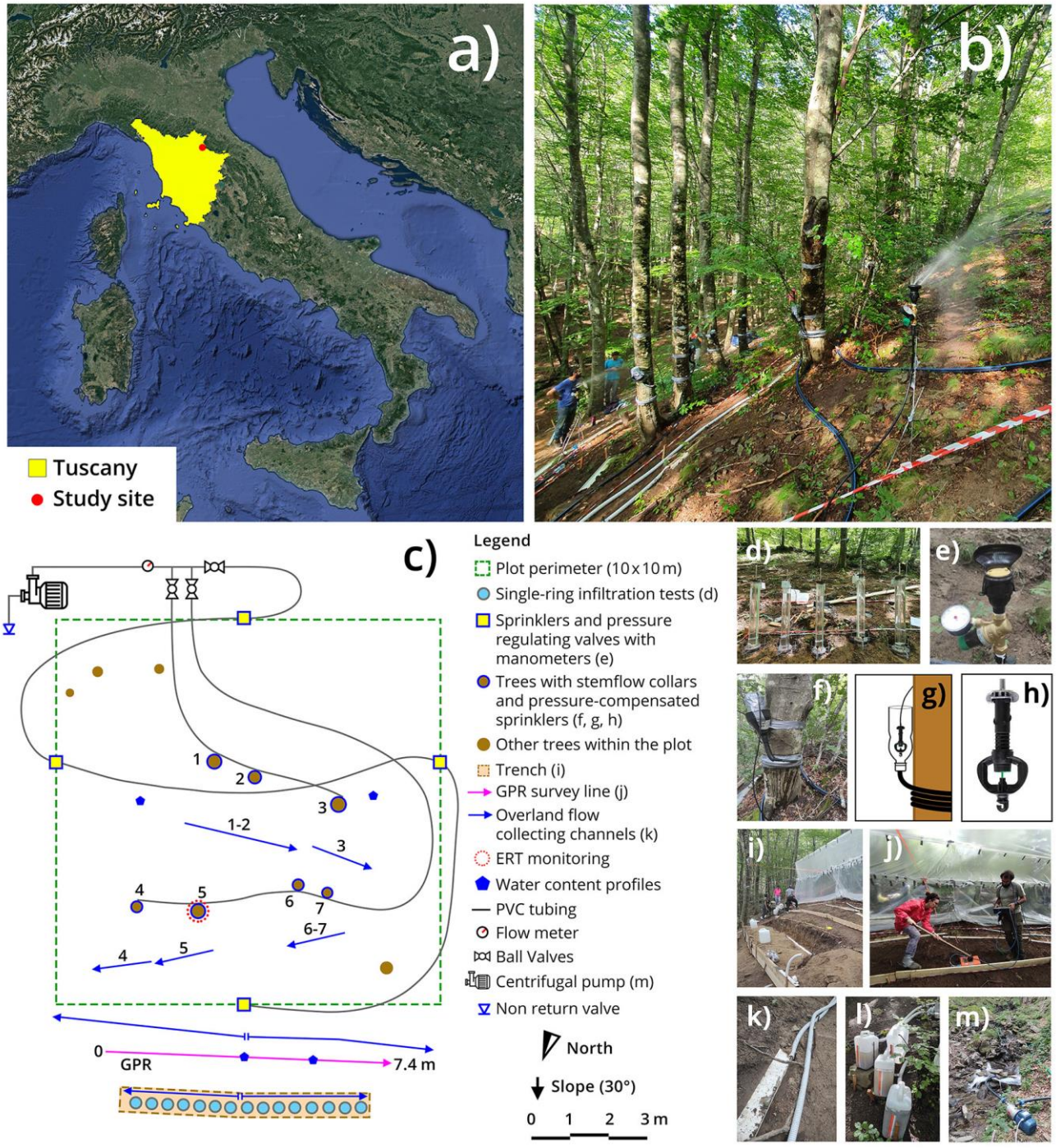

Figure 3. Timeline of stemflow and throughfall simulation events.

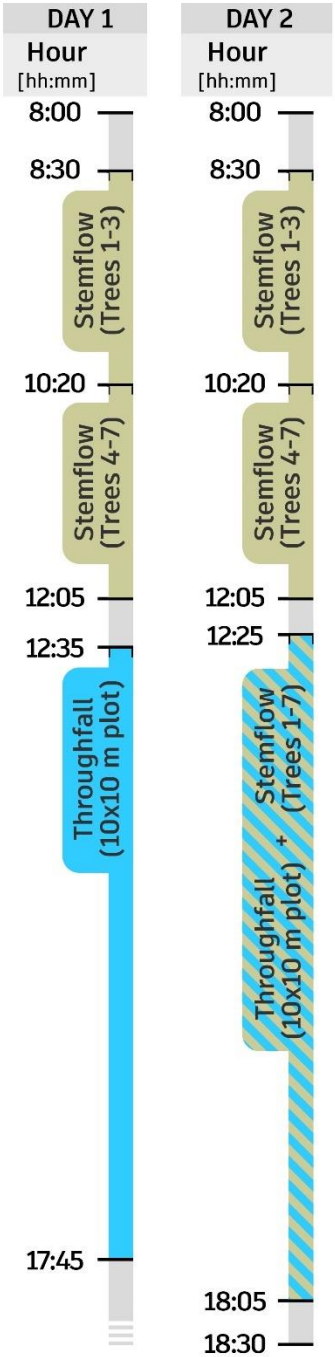

Figure 4. (a, d) Cumulative curves and (b, e) rates of throughfall, stemflow, infiltration, and overland flow processes measured in the afternoon (12:35-5:45 PM and 12:25-6:05 PM) during the two simulation days conducted on the 100 m^2 experimental plot, along with (c, f) the percentages of overland flow and infiltration. Note that on the second day, the throughfall and stemflow simulations were conducted simultaneously.

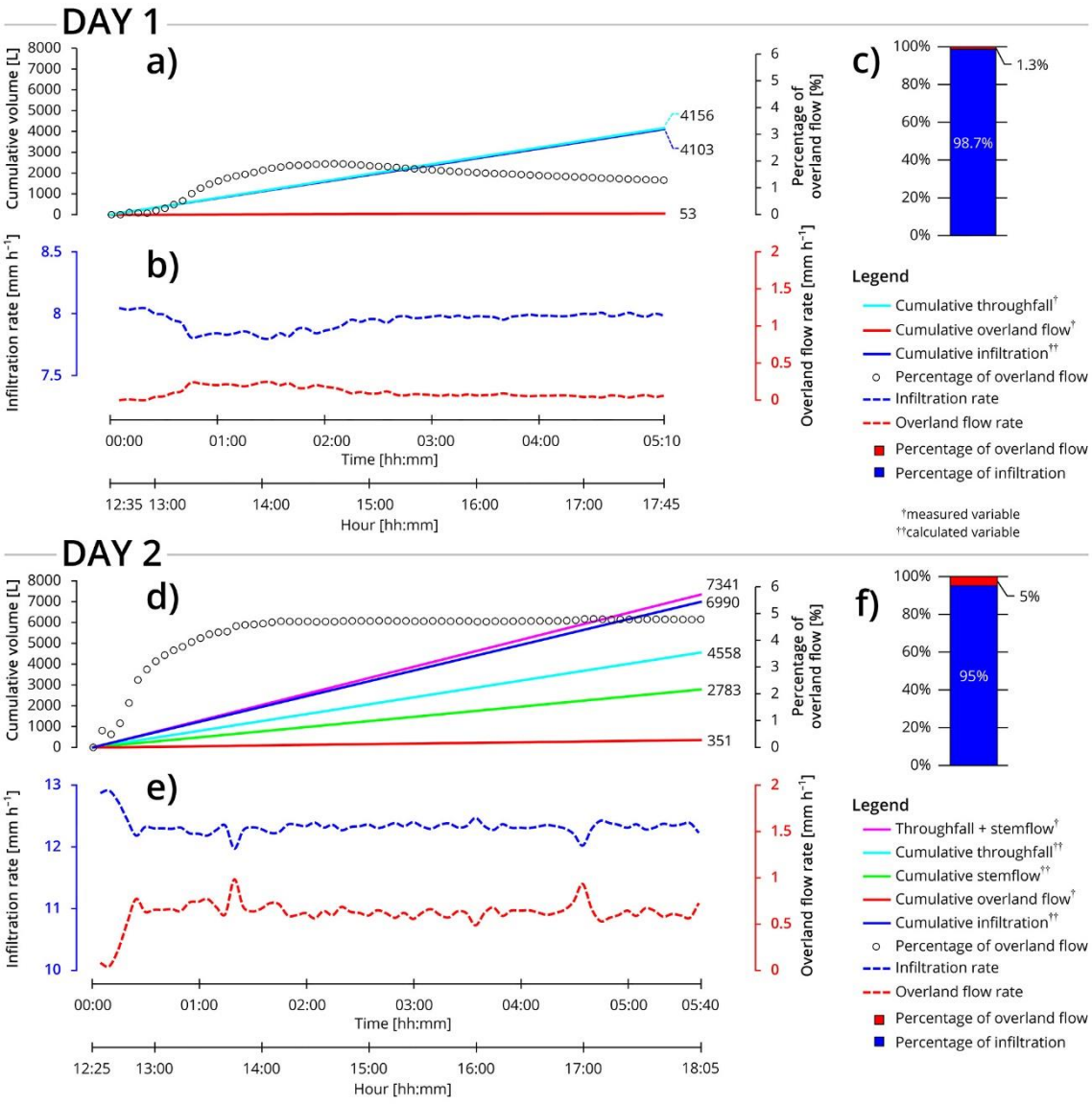

Figure 5. Steady-state stemflow infiltration rates, SIR_{ST} (mm h^{-1}), measured at the (a) tree and 100 m^2 (b) plot spatial scales.

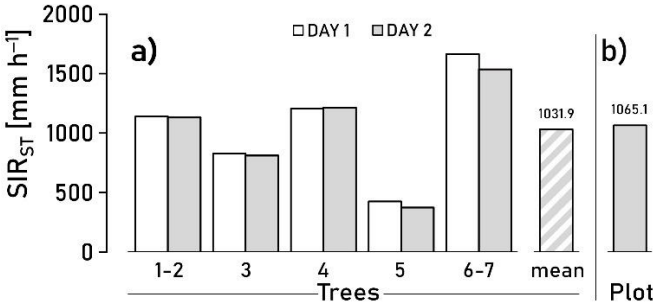

Figure 6. Resistivity changes induced by: (A) stemflow event on Day 1, (B) throughfall event on Day 1, (C) stemflow event on Day 2, and (D) combined stemflow and throughfall events on Day 2.

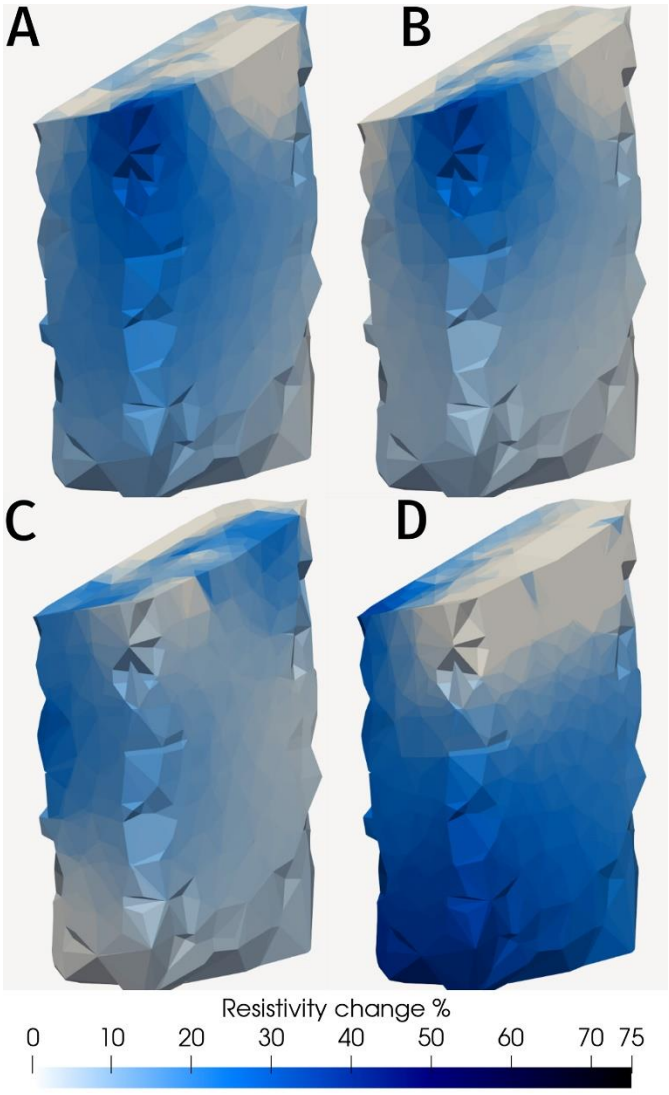

Figure 7. Fitted HYDRUS-1D model and experimental cumulative infiltration curves and infiltration rates measured on the first day (12:35 AM–5:45 PM) during the artificial throughfall event, and on the second day (12:25 PM–8:05 PM) during the artificial throughfall and stemflow events. Throughfall events were conducted on the 100 m^2 plot, while stemflow events were conducted on the seven beech trees.

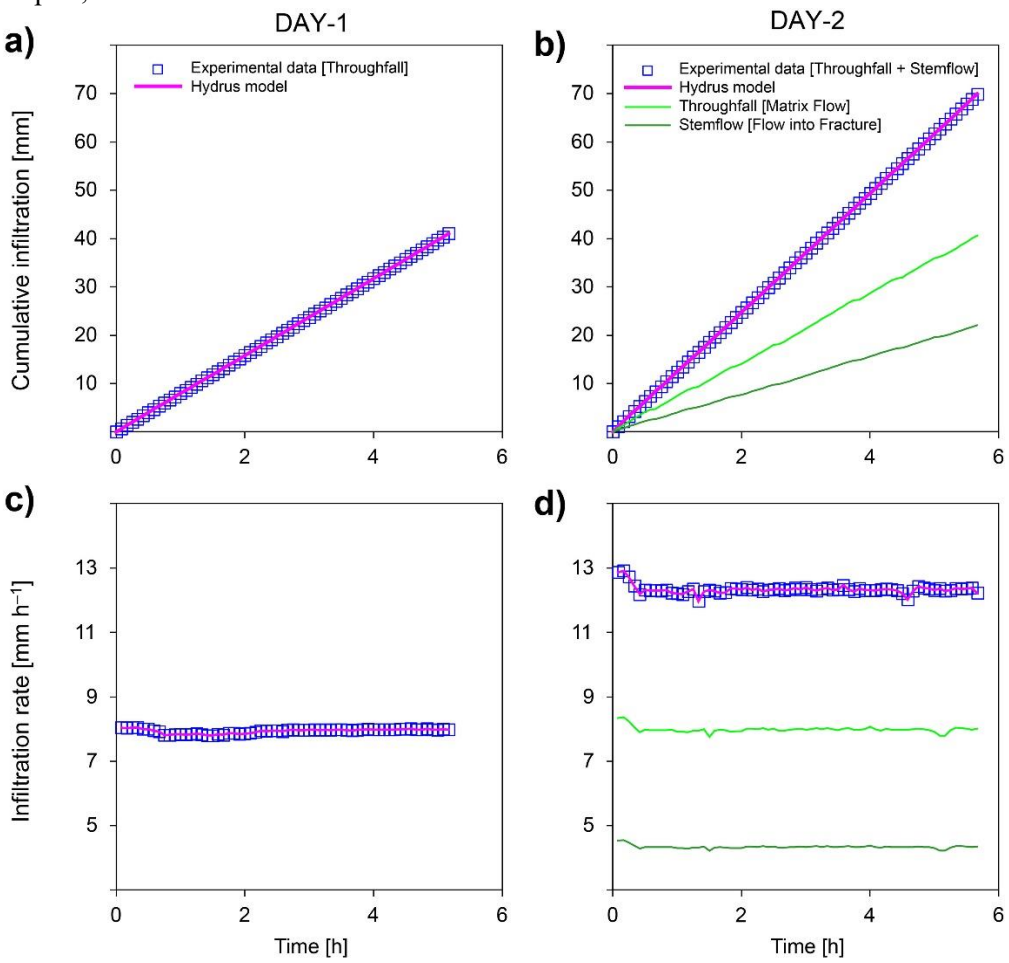

Figure 8. (a) Radargrams acquired before and after the artificial events. The green dashed rectangles highlight the zone of lateral subsurface flow at approximately 1–2.5 m depth, indicated by an increase in amplitude values following imbibition. (b) 3D conceptual model and radargram acquired at the end of the second day. (c) 2D conceptual model.

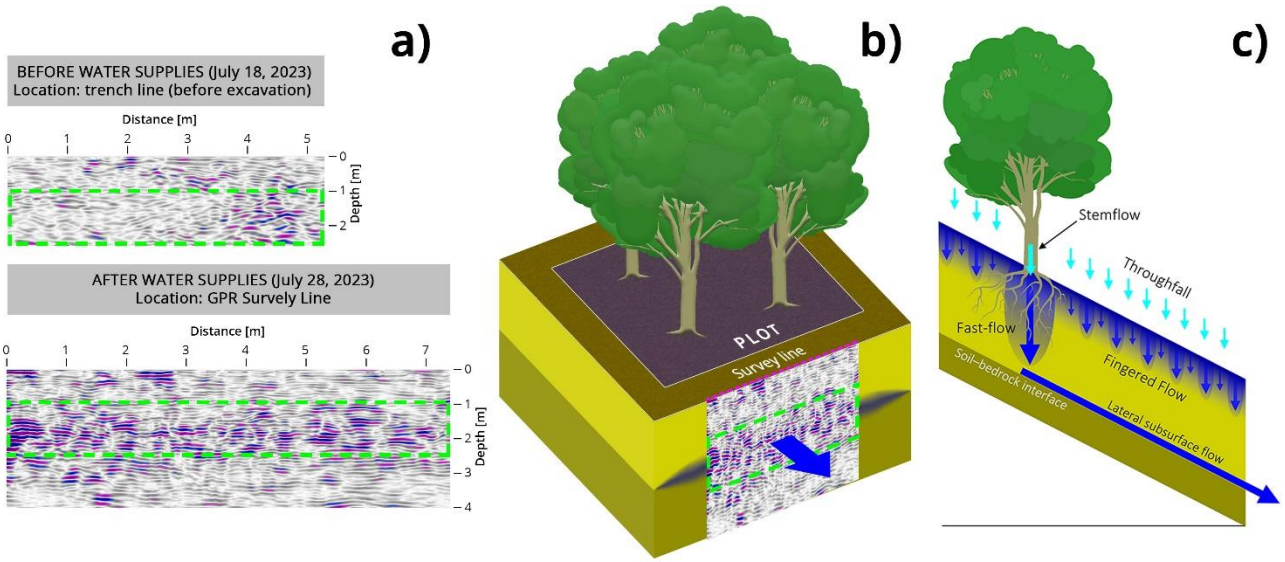

Figure 9. Groundwater level response to precipitation.

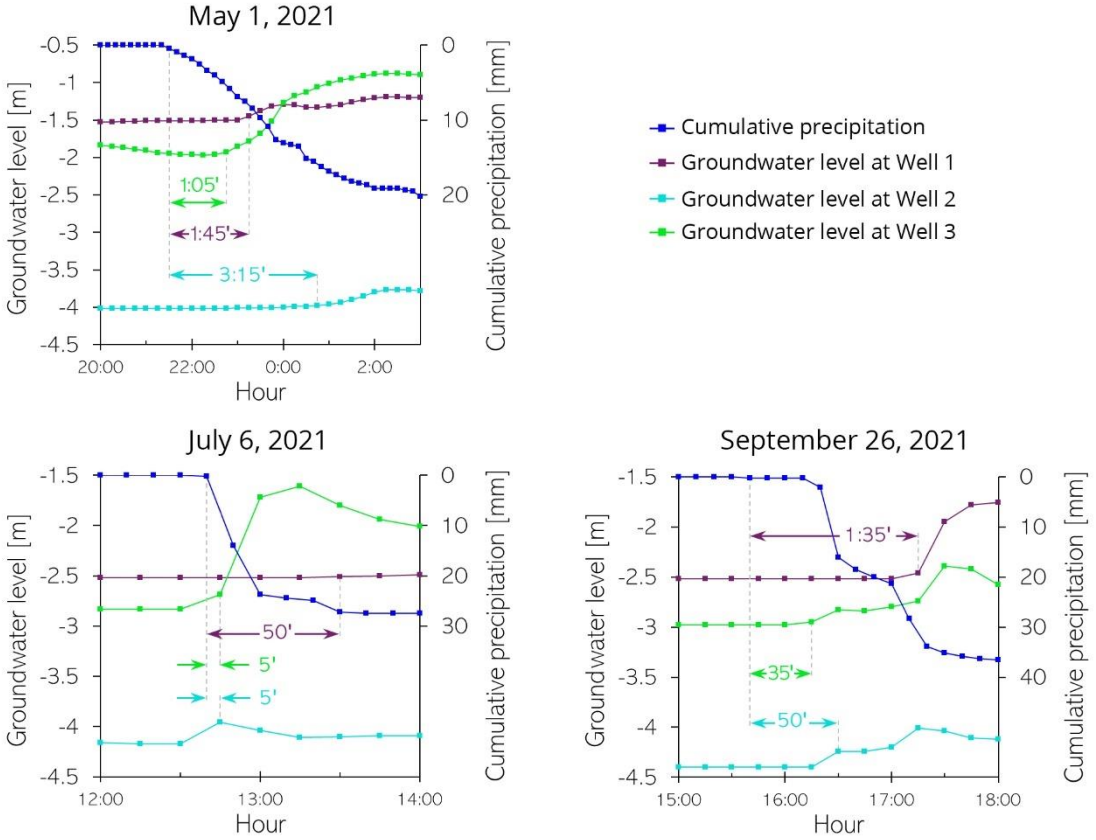

Appendix A. (a) Rainfall exponential functions for different return periods for the Lecciona experimental site (data acquired from the portal of hydrological regional service of the Tuscany region; sir.toscana.it). (b) Water applied during the artificial throughfall events and the corresponding gross rainfall amounts.

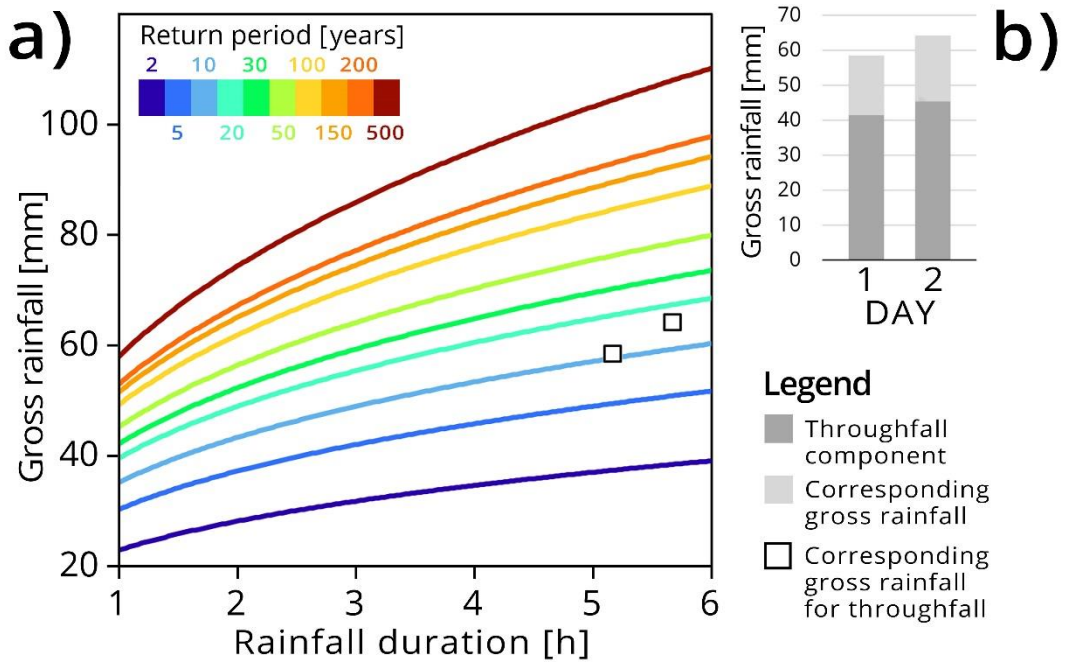

Appendix B. (a) 3D setup and the position of the 72 electrodes (black spheres). The red color highlights zone of maximum sensitivity. (b) Resistivity volume obtained from inversion, representing the dry condition before the beginning of the simulations. The green circle identifies the tree stem position.

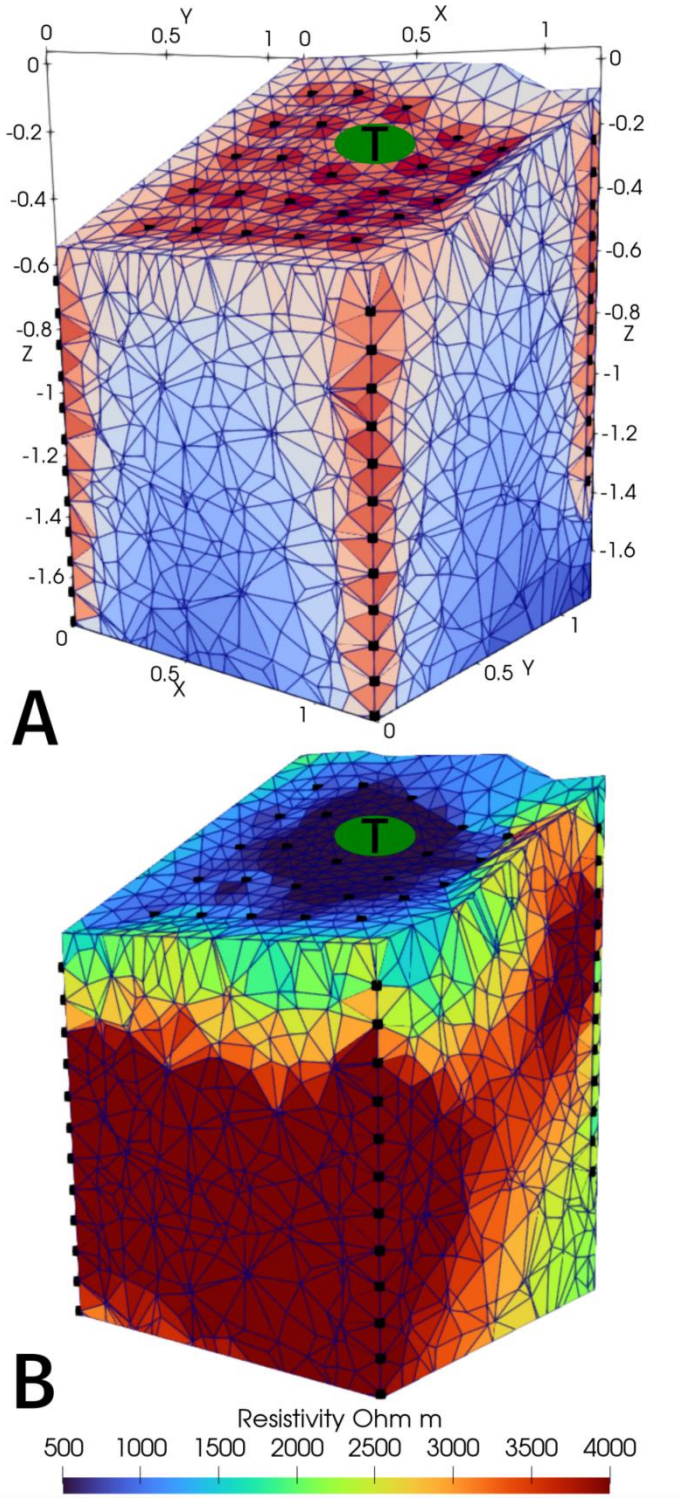

1197

1198 Appendix C. Flowchart illustrating the procedure for retrieving the soil hydraulic parameters using the inverse
1199 option in HYDRUS-1D.

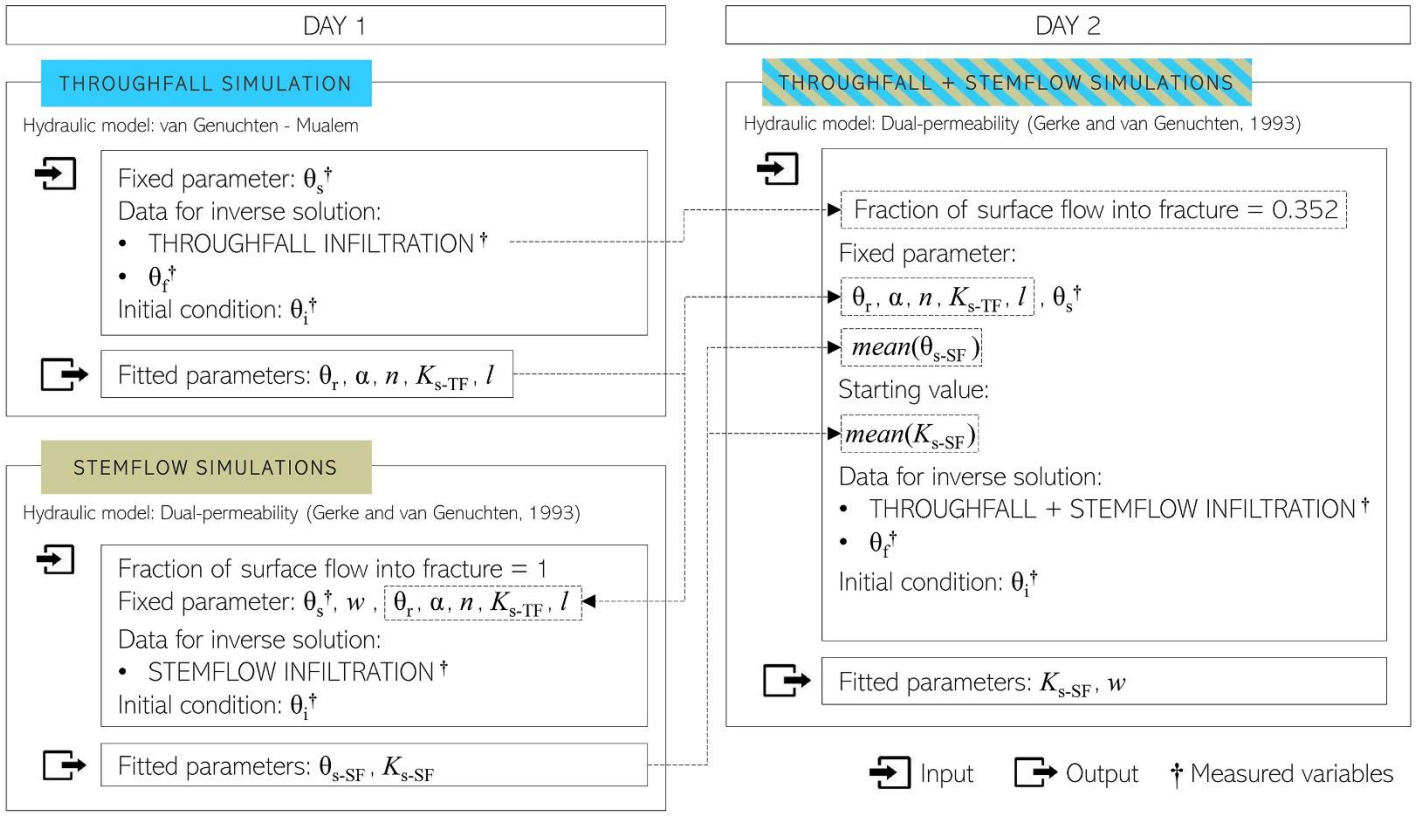

1
1201

Appendix D. (a, c, f, h, k, m, p, r, u, w) Cumulative curves and (b, d, g, i, l, n, q, s, v, y) rates of stemflow, infiltration, and overland flow processes measured in the morning (8:30-12:05 AM) during the two simulation days conducted on seven beech trees, along with (e, j, o, t, x) the percentages of overland flow and infiltration.

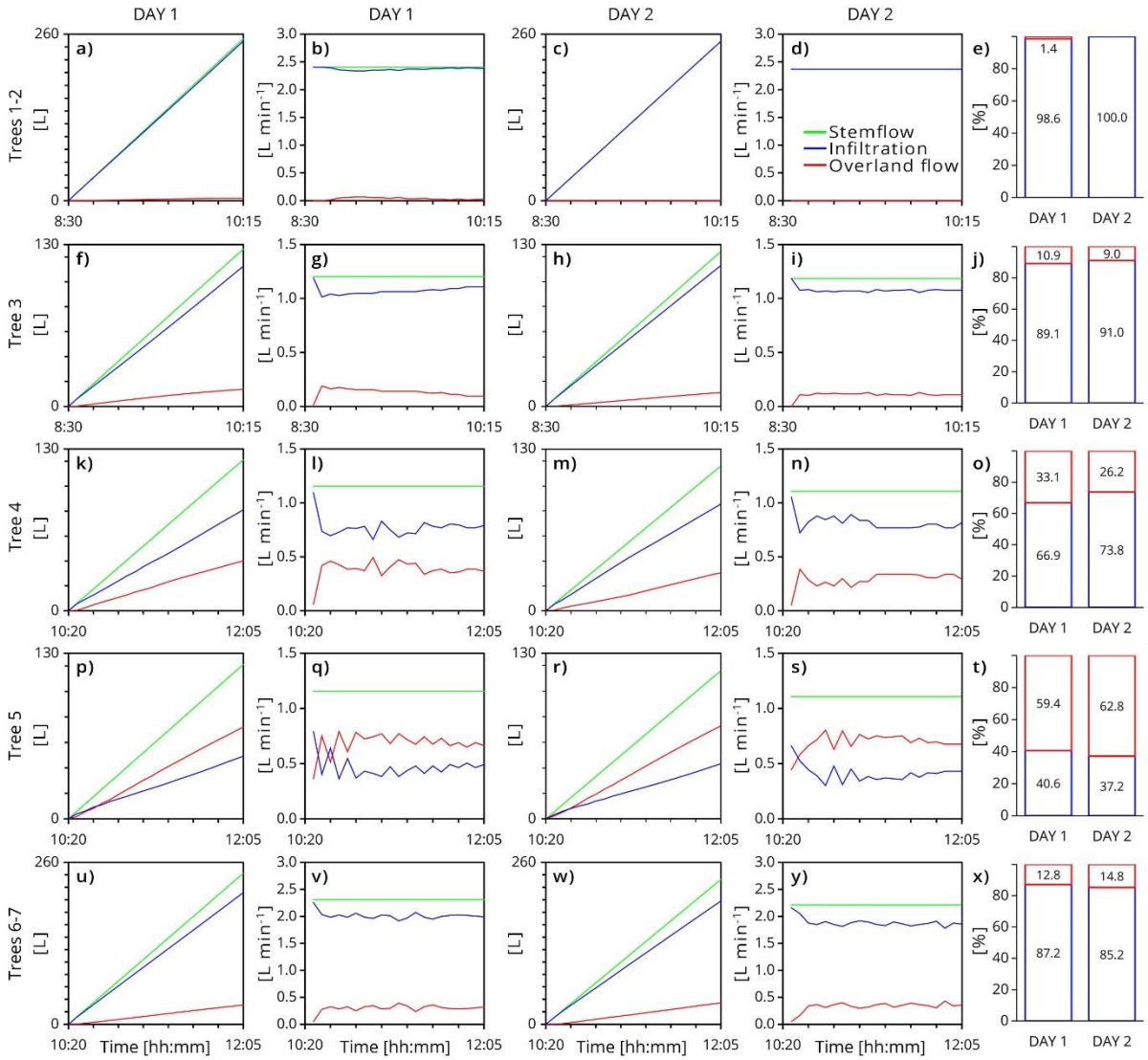

Appendix E. Fitted HYDRUS-1D model and experimental cumulative infiltration curves and infiltration rates measured in the morning of the first day (8:30 AM–12:05 PM) during the artificial stemflow events conducted on seven beech trees.

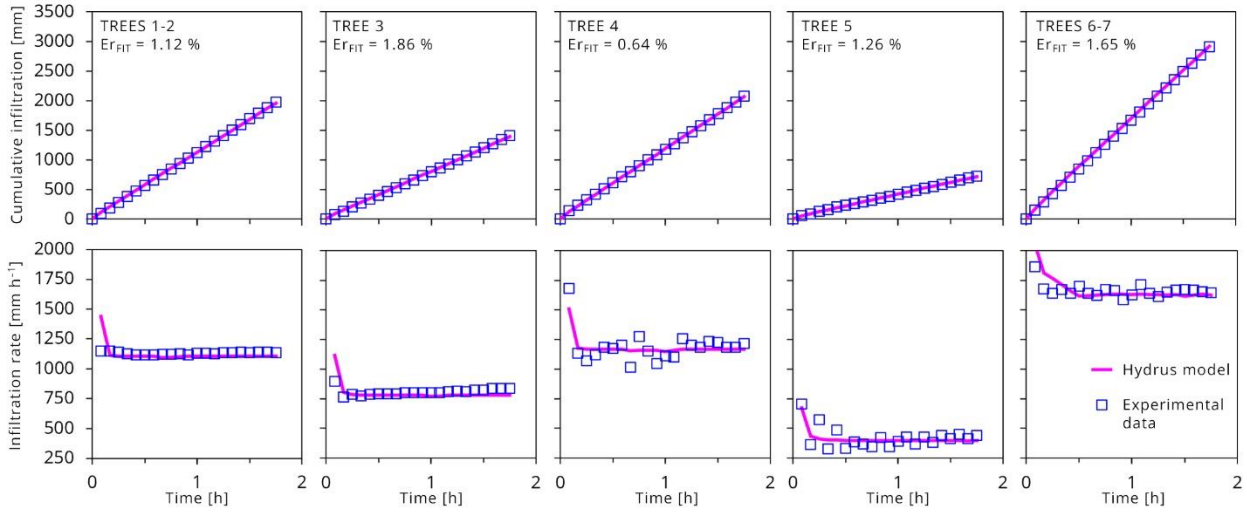

Appendix F. 2D numerical simulation of the stemflow pulse in the morning of the first day at tree 5. (a) Finite element mesh generated for the 2D transect (length: 3 m, depth: 1 m, slope: 30°). White nodes at the boundary represent zero-flux boundary conditions, red nodes indicate stemflow boundary conditions, and green nodes indicate free drainage at the bottom boundary. Water content at (a) 0.875 hours and (b) 1.75 hours from the start of the simulation.

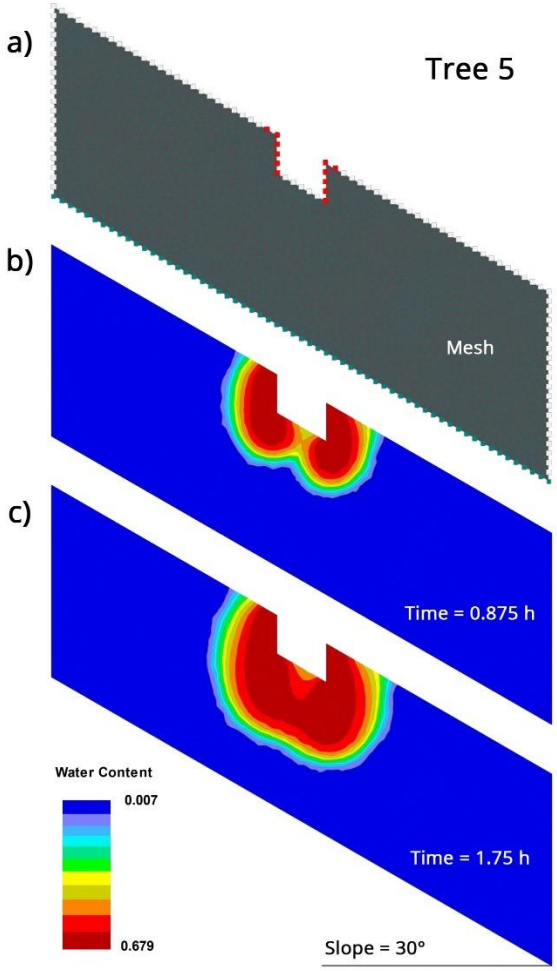

Declaration of Competing Interest

The authors declare that they have no known competing financial interests or personal relationships that could have appeared to influence the work reported in this paper.

Figure 1

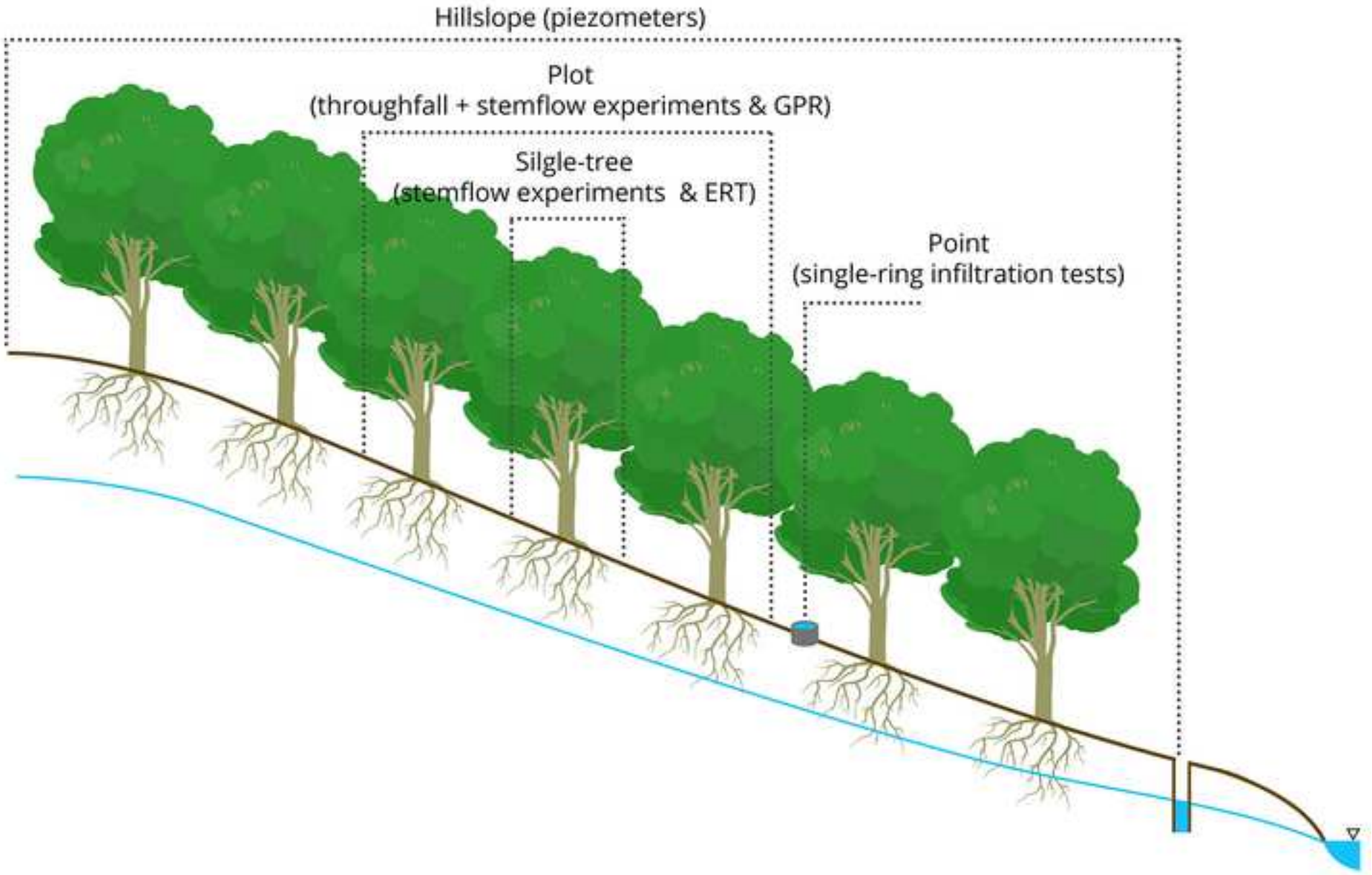

Figure 2

Click here to access/download;Figure;Figure_2.jpg

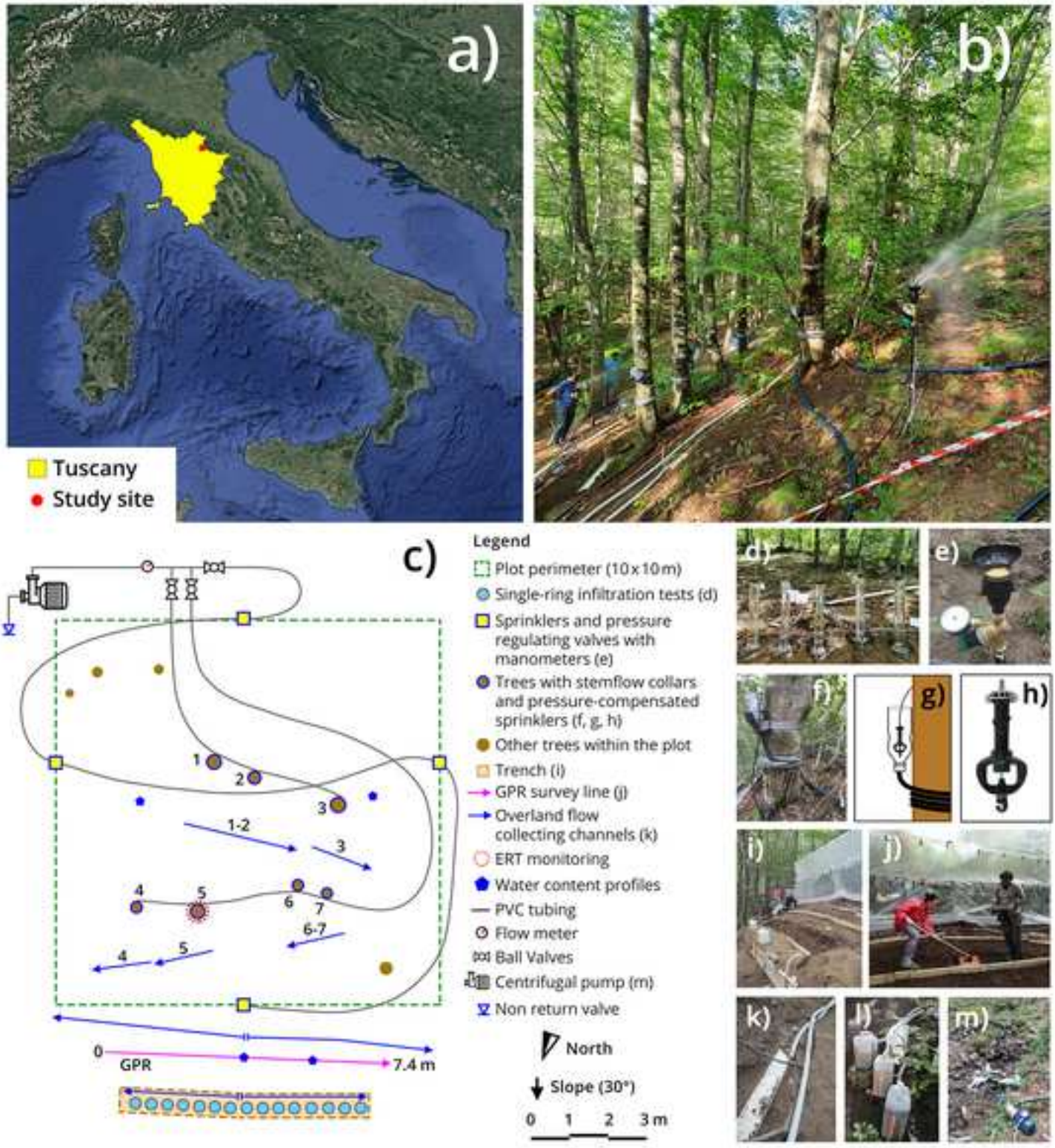

Figure 3

Click here to access/download;Figure;Figure_3.jpg

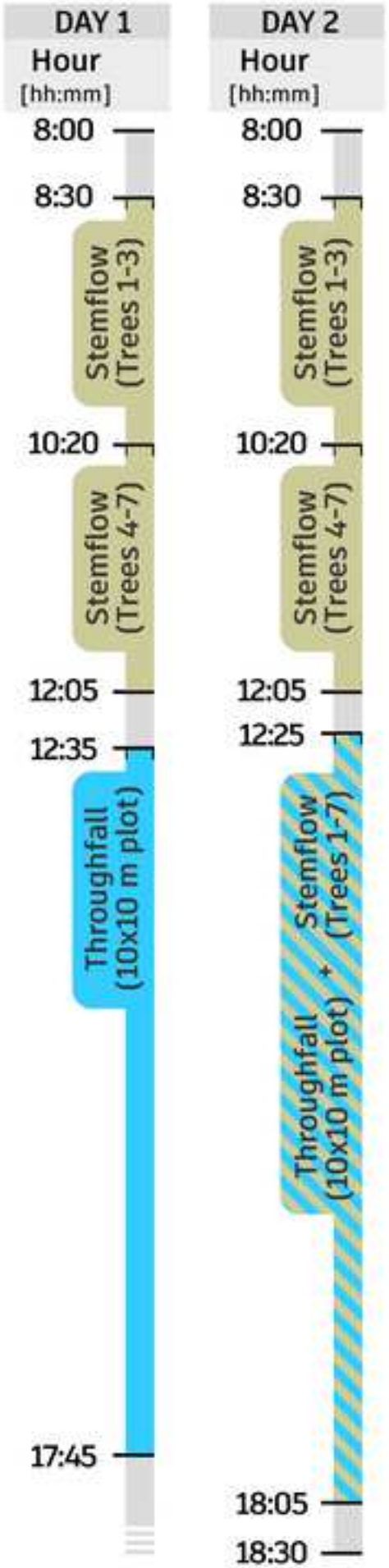

Figure 4

Click here to access/download;Figure;Figure_4.jpg

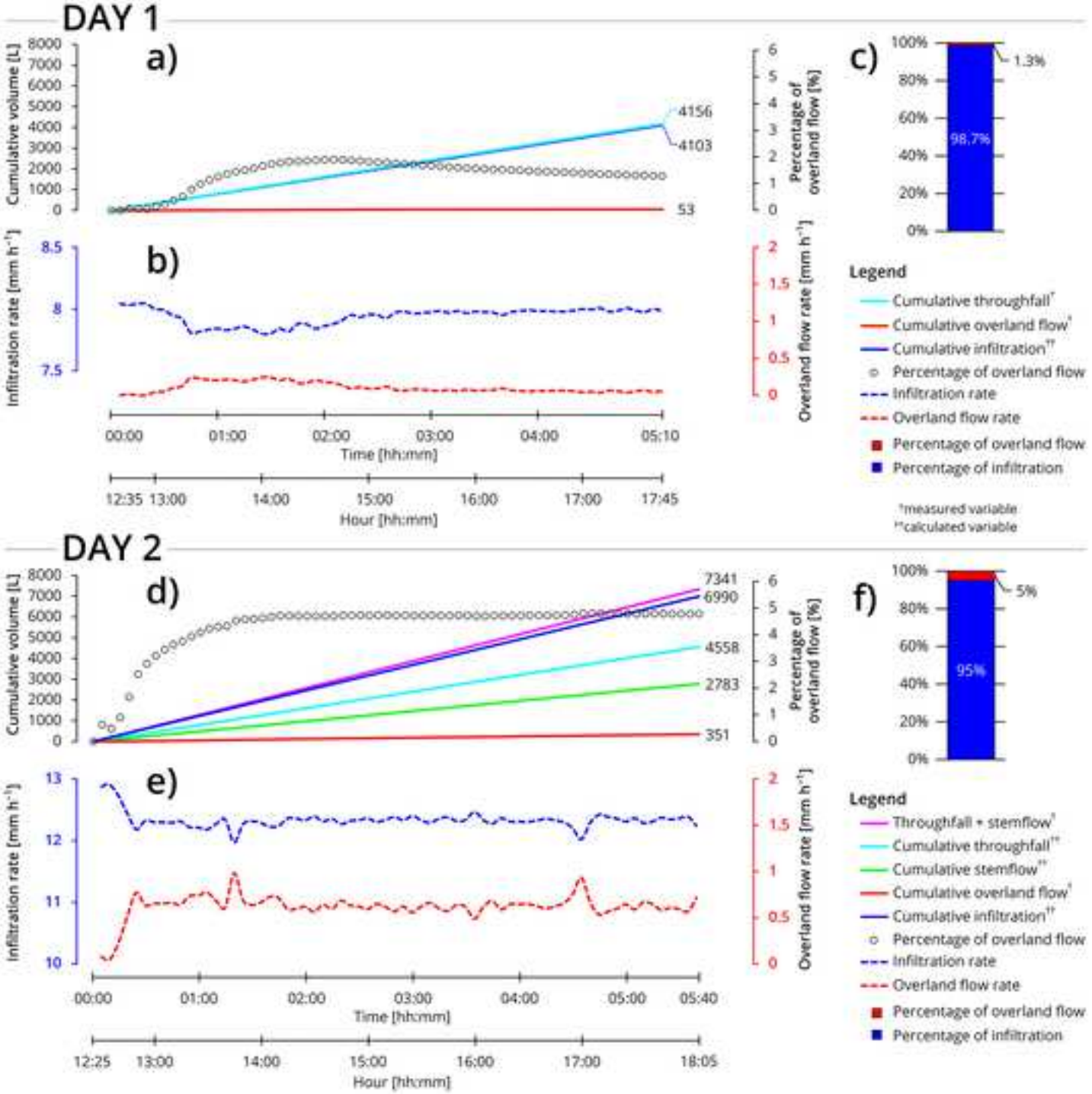

Figure 5

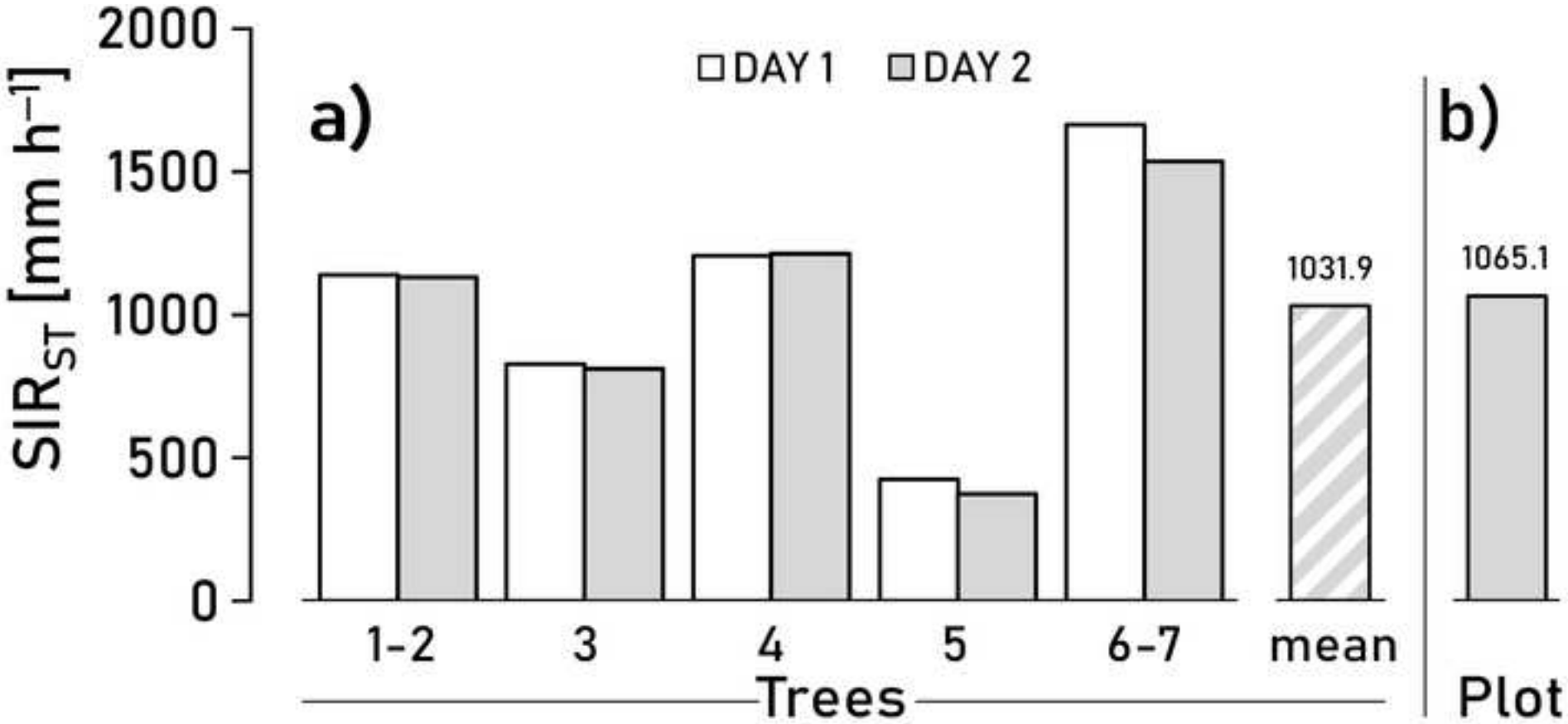

Figure 6

Click here to access/download;Figure;Figure_6.jpg

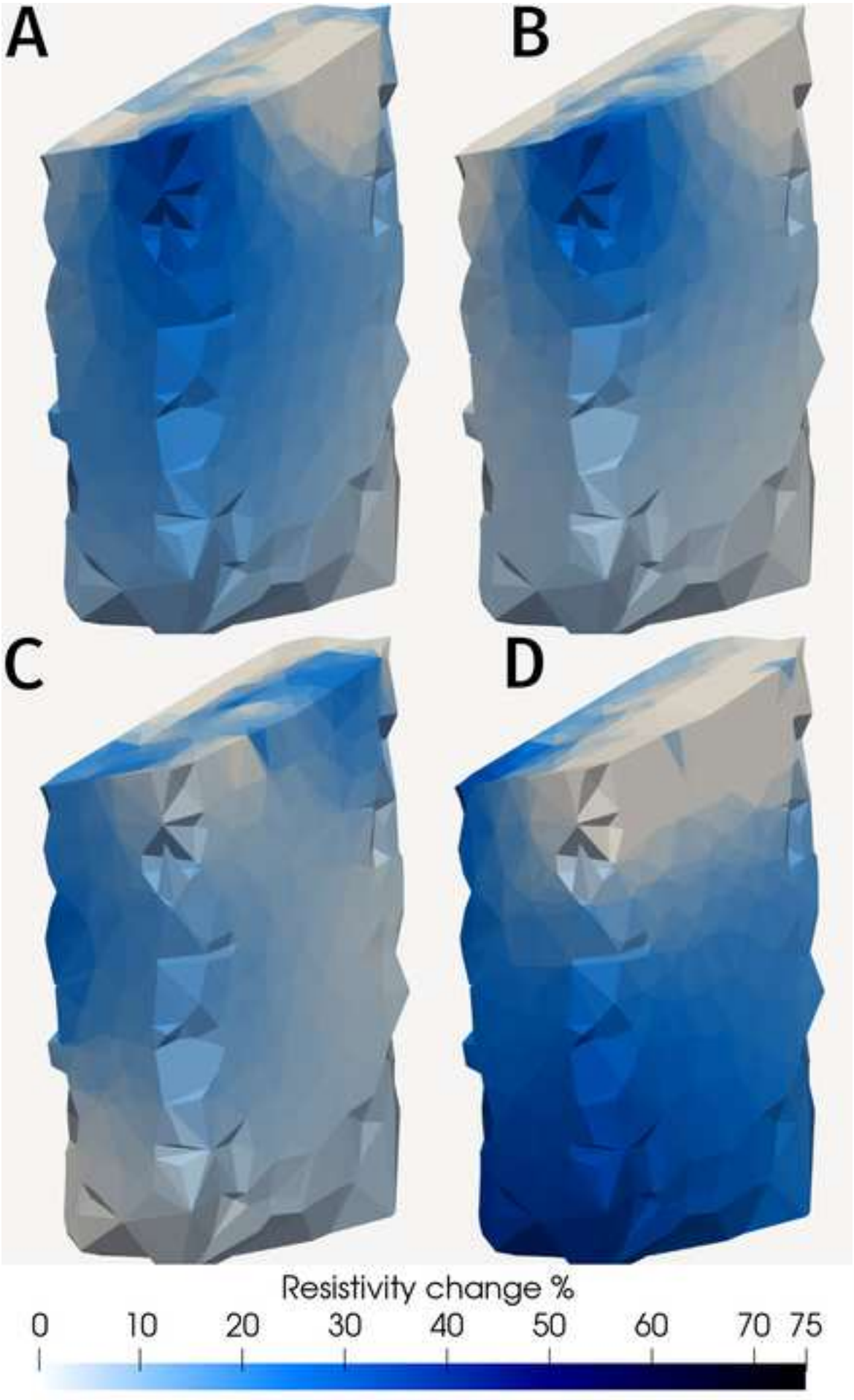

Figure 7

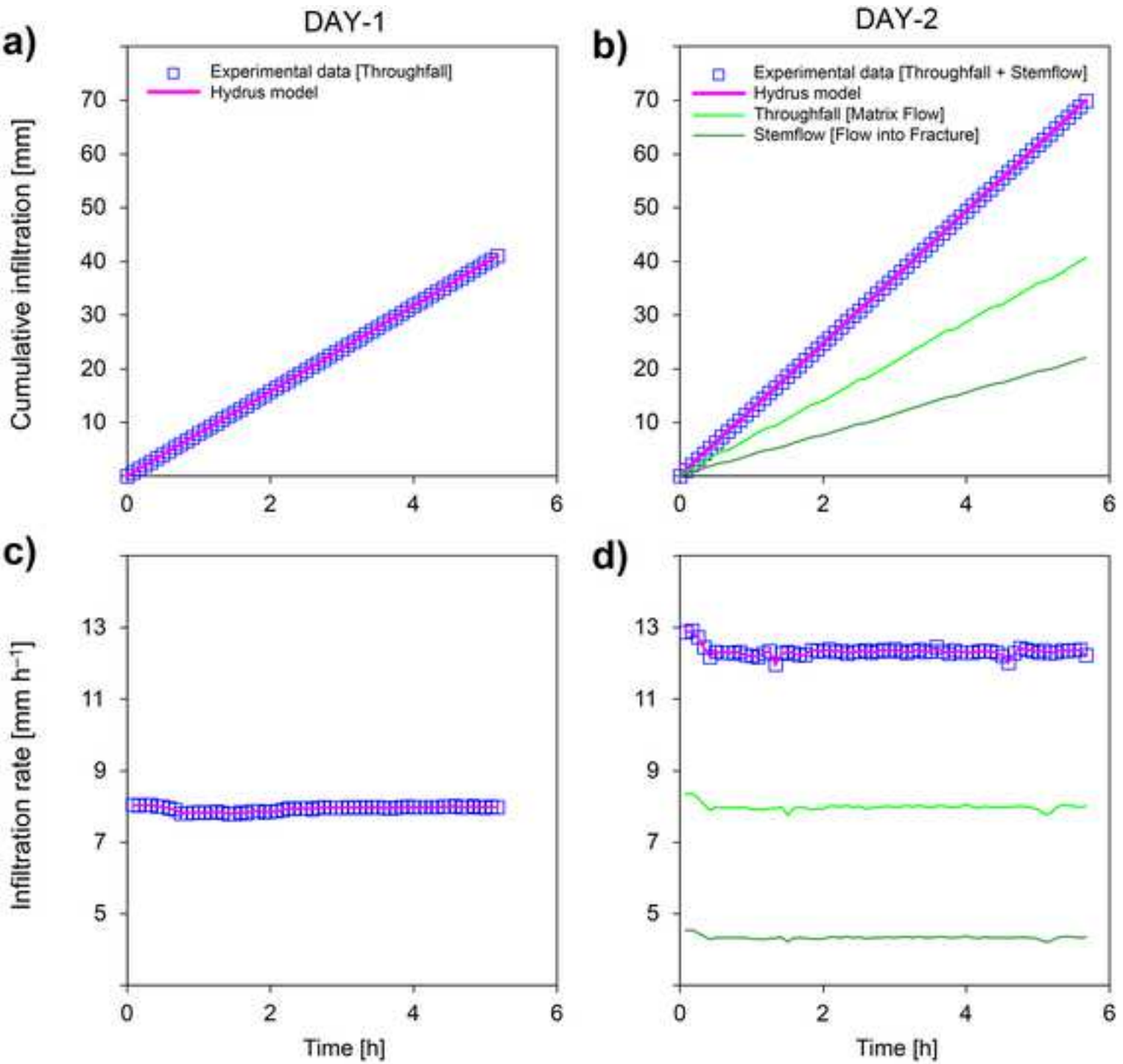

Figure 8

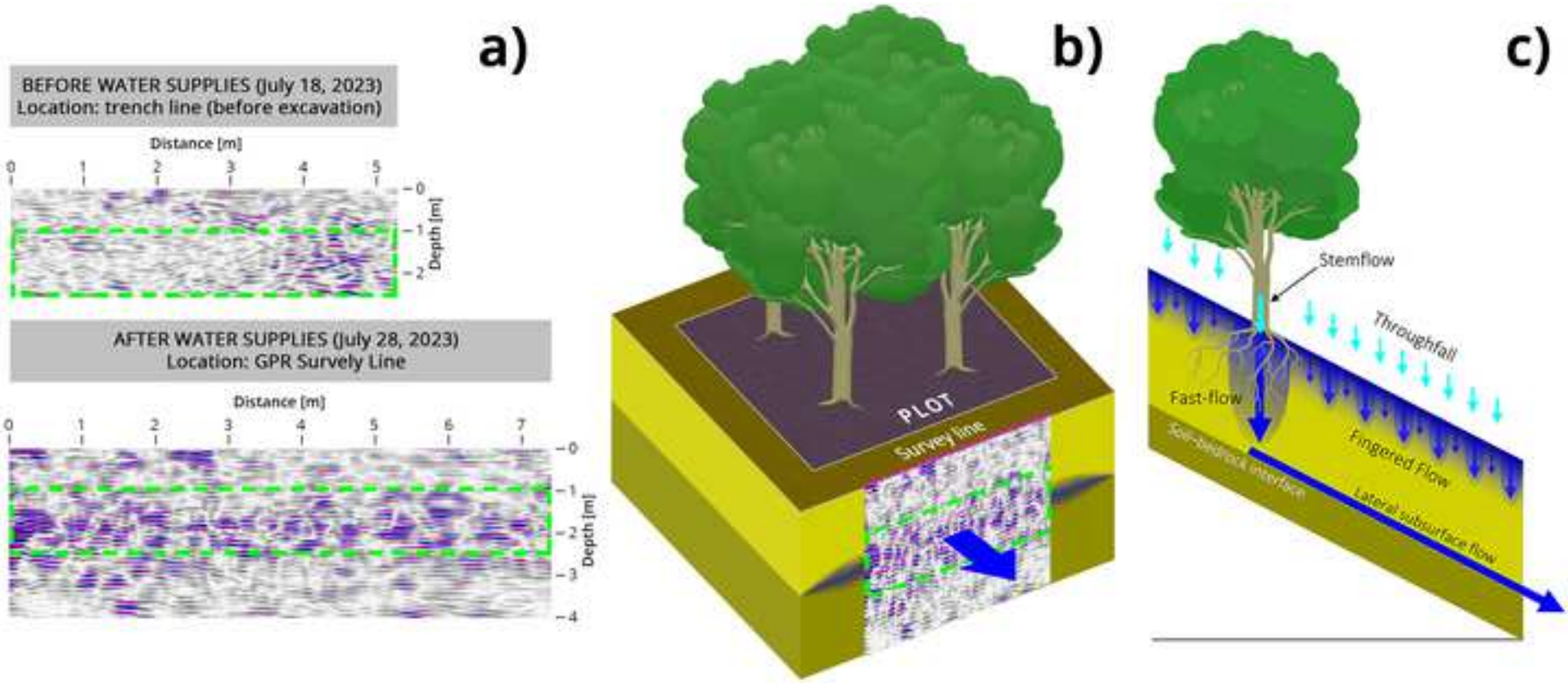

Figure 9

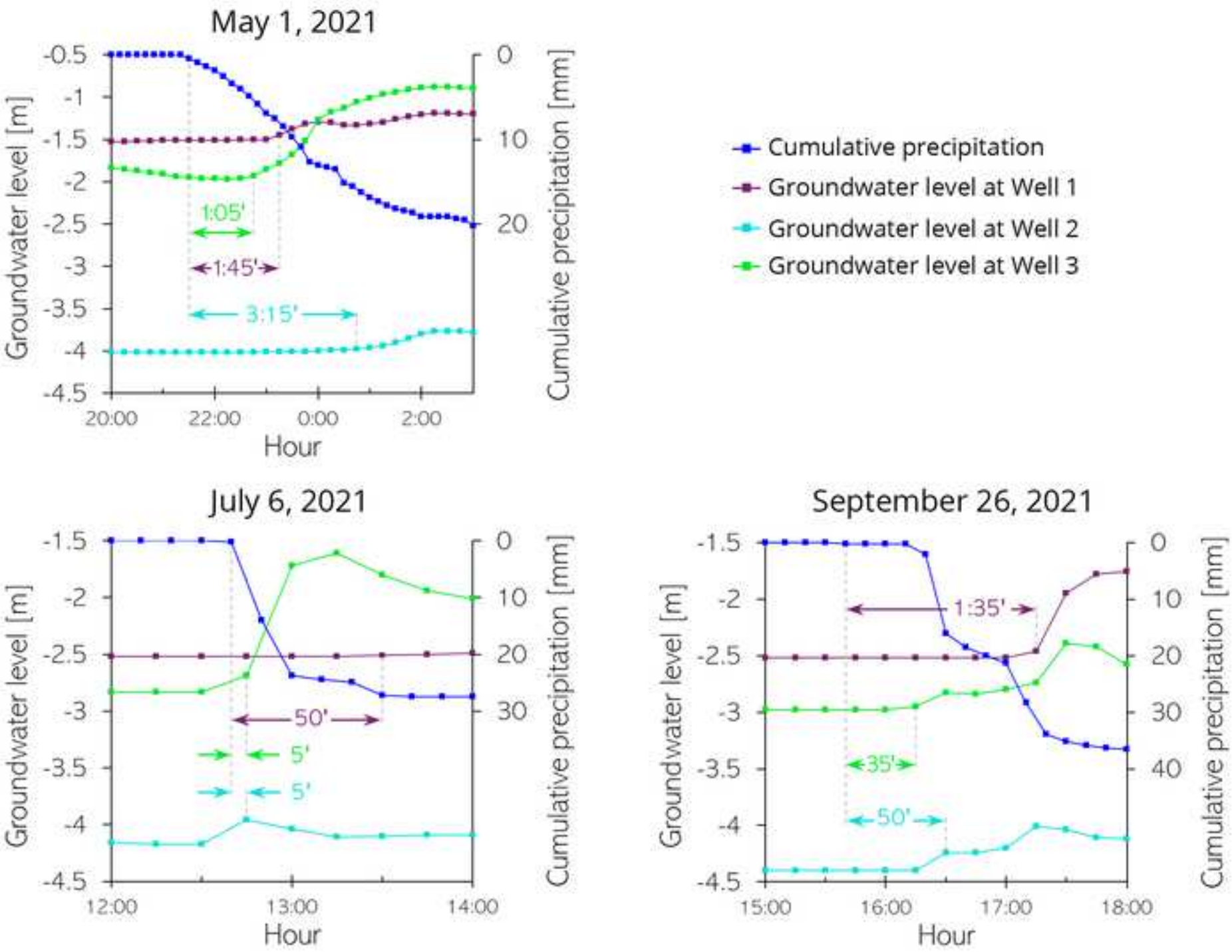

Figure in Appendix A

Figure in Appendix B

Figure in Appendix C

Figure in Appendix D

Click here to access/download

Background dataset for online publication only

Appendix_D.jpg

Figure in Appendix E

Figure in Appendix